2022

Using Multiple Environmental Tracers to Estimate Field-Scale Longitudinal Dispersivity

Casey L. Kleppel
University of Montana, Missoula

USING MULTIPLE ENVIRONMENTAL TRACERS TO ESTIMATE FIELD-SCALE LONGITUDINAL DISPERSIVITY

By

CASEY LEE KLEPPEL

Associate of Science, College of Southern Nevada, Las Vegas, Nevada, 2016
Bachelor of Science, University of Montana, Missoula, MT, 2018

Thesis

presented in partial fulfillment of the requirements
for the degree of

Master of Science
in Geosciences

The University of Montana
Missoula, MT

May 2022

Committee:
Dr. W. Payton Gardner, Committee Chair
Department of Geosciences

Dr. Michael Hofmann, Committee Member
Department of Geosciences

Dr. Jonathan Graham, Committee Member
Department of Mathematical Sciences

Abstract:

In this study, we seek to reduce parameter uncertainty in groundwater modeling systems, particularly in reactive transport models, by quantifying effective field-scale longitudinal dispersivity using anthropogenic environmental tracers. We generate synthetic aquifer fields and model transport of atmospheric tracers and test whether tracers can be used to determine an effective aquifer-scale dispersion coefficient. We generate synthetic datasets by simulating transport of chlorofluorocarbons (CFC11, CFC12, CFC113), sulfur-hexafluoride (SF_6) and tritium (^3H) with input functions derived from known atmospheric concentrations, through a three-dimensional, stochastic, heterogeneous synthetic aquifer developed using sequential Gaussian simulation using the PFLOTRAN reactive transport model. Flux-averaged concentrations calculated from model output are used as synthetic observation datasets to calibrate effective dispersivity for simplified homogeneous models with the PEST parameter estimation software. Tracer-derived effective dispersivity values are compared with theoretical and empirical values reasonable for our stochastic structure. We assess the ability of our homogenous model with tracer-derived effective dispersion coefficients to reproduce transport of a synthetic contaminant through the heterogeneous 3D field with two new boundary conditions. The ratio of CFC11/SF_6 displays less than a 10% difference between the full (4.12m) and single-time (4.43m) series derived effective dispersivity. The ratio of CFC12/SF_6 displays less than a 10% difference between the full (4.09m) and single-time (4.43m) series value. While all tracer-derived values from both the full-time and single-time series (1.96 m to 10.75 m) were within reason compared to the theoretically and empirically derived values (1.01 m to 5.32 m), dispersivity values derived from CFC11/SF_6 and CFC12/SF_6 for the full and single-time series display quantitatively smaller residuals compared to our heterogeneous truth model for our new boundary conditions. Our results indicate that environmental tracers can be useful in estimating effective dispersion coefficients for reactive transport models over longer length and time scales than traditional applied tracer studies. This new method of utilizing multiple environmental tracers over a limited time series could be an easy, inexpensive, and effective solution in quantifying field-scale longitudinal dispersivity and reduce parameter uncertainty in groundwater/contamination transport models.

1. Introduction

Understanding how groundwater and dissolved solutes propagate through an aquifer system due to complex subsurface heterogeneous structure is critical in developing models that more accurately simulate subsurface systems. The main source of uncertainty within all groundwater transport models is in the implementation of parameter values that accurately characterize the system (Gupta et al., 2012). Because the exact complexity of any subsurface system is unknown, parameter values are often assumed and rarely quantified at the required resolution. Beginning with the conceptual model of the system and continuing through the numerical analysis, these assumptions underlie all resulting model simulations and developed conclusions. A systematic way to reduce parameter uncertainty in any model is to collect as much information as possible about the system that is trying to be reproduced (Bredehoeft, 2005).

Many transport models use an implementation of the advection-dispersion equation that takes into account advection, mechanical dispersion and diffusion (Sudicky, 1988). Hydrodynamic dispersion is the combined effect of unknown, random fluctuation in groundwater velocity (mechanical dispersion) and molecular diffusion. This dispersion parameter is essential in describing how solutes spread due to heterogeneity and associated variation of groundwater velocity and is assumed to be a unique property of geologic mediums (Bear and Bachmat, 1967). Transport of solutes in the subsurface displays variations in flow velocity due to this heterogeneity and these migration pathways are important in developing a more complete understanding of contaminant migration transport (Novakowski et al., 1985).

There are three main methods to quantify longitudinal dispersivity: lab-scale core injection tests, field-scale injection tests and field-scale quantification of heterogeneity through analytical solutions and stochastic analysis. The largest disparity between these methods is the scale at which they are performed. Field-scale dispersivity investigations find dispersivity values that are several orders of magnitude larger than lab-scale values for the same porous material (Gelhar et al., 1992). Packed, structured porous columns fail to adequately represent full field heterogeneities due to inconsistent parameterization as a function of distance (Khan and Jury, 1990). Core scale laboratory dispersion experiments

cannot be used to measure field-scale dispersivity values because dispersivity values increase with transport distance in groundwater systems (Gelhar et al., 1992; Pang and Hunt, 2001)

In field-scale injection tracer experiments, a known concentration of tracer is injected, and the concentration tracked throughout the site over spatial and temporal scales of interest. Injection and monitoring well installation, field-site access or regulations, and the time involved to perform tracer testing are prohibitive and lead to small-scale site experimentation to infer large-scale site characteristics. Injection tracers experiments are limited to small-scale site experiments, can be subject to error due to insufficient monitoring points, are limited by the amount of time the experiment can be conducted, often only quantify short flow path lengths, and are very expensive to run (Sudicky and Illman, 2011).

Environmental tracers are natural or anthropogenic compounds that are globally distributed in the Earth's hydrologic cycle, and their concentrations within subsurface systems can be used to determine pathways and time cycles of environmental processes (Cook, 2000). An ideal tracer is mobile and soluble, whose movement is not strongly retarded by the aquifer matrix, has known atmospheric concentrations and has a well-known input history (event markers) (Cook, 2000). These environmental tracers are ambiently applied to the natural system globally in all subsurface settings due to the hydrologic cycle at known times and move through all subsurface systems as a function of longitudinal dispersivity. Environmental tracers are currently implemented to quantify aquifer parameters such as vertical and horizontal flow velocities, historical changes in solute and contaminant loads to systems, estimation of solute transport velocities, measurements of timescales for subsurface chemical reactions, and determination of mean groundwater ages through different numerical modeling techniques (Zhang, 1996; Cook, 2000; Leray et al., 2012; Chambers et al., 2018). To date, directly measured CFC and SF_6 concentrations are not currently utilized to constrain longitudinal dispersivity. CFC and SF_6 tracer concentrations are ideal for measuring longitudinal dispersivity values due to their long-term input at known rates over large temporal and spatial scales into groundwater systems through the hydrologic cycle, exhibit low solubility in water, and move through global groundwater systems as a function of longitudinal dispersivity.

Tritium has proven to be a useful environmental tracer to quantify longitudinal dispersivity at the field scale because it forms part of the water molecule, travels with groundwater and is present in groundwater that is younger than 60 years old (Jensen et al., 1993; Gardner et al., 2011) . The distribution of ^{3}H over time on a flat-laying delta of the Sturgeon River in Sturgeon Falls, Ontario, Canada was used to quantify groundwater recharge rates and longitudinal dispersion values over short flow lengths near the water table by solving 1 and 2 dimensional models to create synthetic ^{3}H distributions and varying the parameter of dispersivity in order to minimize the error between simulated and observed data (Robertson and Cherry, 1989). The Canadian Forces Base Borden site is home to the best-known hydrodynamic dispersion experiment to constrain dispersivity parameters and observe contaminate plume migration in a shallow alluvial aquifer system. Through a series of tritium (^{3}H) sampling, injection tracer experiments, one-dimensional advection-dispersion simulations, and comparison of observed data to synthetic geostatistical modeling, longitudinal dispersivity values were quantified (Egboka et al., 1983; Sudicky, 1988). The hydrodynamic dispersion parameter values that gave the least error between the observed and modeled data are in the range of approximately 30 – 60 meters (Egboka et al., 1983). Large-scale horizontal transport parameters were estimated in a sandy aquifer in Denmark quantified by fitting ^{3}H breakthrough curves with analytical advection dispersion models (Jensen et al., 1993). All three experiments used a time series of tritium concentrations, with peak concentrations of tritium being introduced into the system from hydrogen bomb testing in the 1950's and 1960's (Figure 1). Tritium has a half-life of 12.3 years and the anthropogenically introduced concentrations from bomb testing is almost completely decayed out of our system, which implies that other environmental tracer techniques would be useful (Cook, 2000).

In this work, we quantify longitudinal dispersivity by using a suite of environmental tracer concentrations and compare observed tracer-derived dispersivity values to dispersivity values calculated from theoretical and empirical equations. We develop a new method of using CFCs and SF_6 concentrations and concentration ratios of CFC11 and CFC12 over SF_6 to constrain a field scale value of longitudinal dispersivity. This new method of using these ratios mimics a distinct concentration peak analogous to the tritium

concentrations that are naturally decaying out of subsurface systems. We then assess the ability of tracer-derived longitudinal dispersivity values to predict contaminant transport. This work improves our understanding of the influence of subsurface heterogeneities on contaminant fate and transport, develops a new implementation of environmental tracer concentrations, and develops transport models simulating real-world subsurface characteristics to make better forecasts of groundwater contaminant transport fate.

2. Research Question & Hypothesis

Research Question:

Can multiple environmental tracer concentrations (e.g., ^{3}H, CFCs and SF_6) sampled a limited number of times quantify effective longitudinal dispersivity in groundwater systems?

Hypothesis:

We hypothesize that incorporating a suite of environmental tracer concentrations sampled over limited spatial and temporal scales directly into reactive transport models can be used to quantify field-scale values of longitudinal dispersivity and reduce parameter uncertainty.

- Properties of environmental tracers are ideal for evaluating this hypothesis because they are ubiquitously applied globally to the natural system through the hydrologic cycle.
- The most up-to-date atmospheric concentrations of these tracers can be obtained through NOAA.
- Environmental tracers introduced to subsurface systems through the hydrologic cycle function as a long-term injection tracer test moving through the aquifer systems as a function of longitudinal dispersivity.

3. Theory

Solute transport equations

The classic model for solute transport in subsurface systems is the advection-dispersion equation. This equation encompasses the processes of advection, molecular diffusion, and mechanical dispersion. The advection-dispersion equation for 3D transport is:

$$\frac{\partial C}{\partial t} = \left[D_x \left(\frac{\partial^2 C}{\partial x^2}\right) + D_y \left(\frac{\partial^2 C}{\partial y^2}\right) + D_z \left(\frac{\partial^2 C}{\partial z^2}\right)\right] - \left[\bar{V}\left(\frac{\partial C}{\partial x}\right) + \bar{V}\left(\frac{\partial C}{\partial y}\right) + \bar{V}\left(\frac{\partial C}{\partial z}\right)\right] - KC \quad (1)$$

where x, y, and z are the distance along a streamline with respect to the input zone, *t* is time, C is concentration, $D_{(x, y, z)}$ are the coefficients of hydrodynamic dispersion with respect to their spatial component of flow velocity, V is the average linear groundwater velocity, and K is the radioactive decay constant for a given tracer (Bear, 1972).

The coefficient of hydrodynamic dispersion is defined in Cartesian tensor notation as:

$$\overline{D_{ij}} = \alpha_{ijkl}\frac{v_k\, v_l}{|v|} + D'_m, \; i, j, k, l = 1, \ldots n_d \quad (2)$$

where $\overline{D_{ij}}$ is the coefficient of hydrodynamic dispersion, α_{ijkl} is the dispersivity of the porous medium (a fourth-order tensor), v_k and v_l are the spatial components of flow velocity, n_d is the number of spatial dimensions, D'_m is the coefficient of diffusion in a porous medium, D_m, over the effective porosity, n_e, and $|v|$ is the magnitude of the velocity vector (Ingebritsen and Sanford, 1998). The dispersivity coefficient contains 81 components in three-dimensional space, but symmetry properties, even in the case of an anisotropic porous medium, will reduce the number of components to 36 (Konikow and Grove, 1977). For an isotropic porous medium, the number of dispersion coefficients can be defined by two constants, both described in units of length (Ingebritsen and Sanford, 1998). The first coefficient is longitudinal dispersion, α_L, which describes the dispersivity of a porous medium parallel to groundwater flow (Scheidegger, 1961). The second coefficient is transverse dispersivity, α_T, which describes the dispersivity of a porous medium transverse to the direction of groundwater flow (Scheidegger, 1961). Transverse dispersivity can be further broken down into horizontal transverse dispersivity that describes spreading in the horizontal direction perpendicular to horizontal flow, and

vertical dispersivity due to the effect of heterogeneity in the vertical direction, but both horizontal and vertical transverse dispersivity are commonly assumed as the same coefficient (Bear and Bachmat, 1967). The value of horizontal transverse dispersivity can be considered as one order of magnitude lower than longitudinal dispersivity, and the vertical transverse dispersivity can be considered two orders of magnitude lower than longitudinal dispersivity (Gelhar et al., 1992). The coefficient of hydrodynamic dispersion can be decomposed further as:

$$D_x = \alpha_L \bar{V} + D^* \quad (3)$$

where α_L is the longitudinal dispersivity and D^* is the coefficient of molecular diffusion for the specific chemical species in the porous medium (Egboka et al., 1983). Longitudinal dispersivity (α_L) is the key parameter that describes the local variations in the velocity field of a solute in groundwater systems in the direction of flow, and is a fundamental parameter needed for defining transport of groundwater contaminants.

Richards' equation is used to describe groundwater flow in single phase, variably saturated systems and can be described as:

$$R = \frac{\partial}{\partial t}(\theta \rho_w) + \nabla * p_w q_w$$
$$q_w = \frac{-k k_r}{\mu} \nabla (P - \rho_w g z) \quad (4)$$

where R is the internal water source or sink (L/T), ρ_w is the density of water (M/L^3), P is the fluid pressure (F/L^2), k is the intrinsic permeability of the porous medium (L^2), μ is the viscosity of water (M/L/T), g is the gravitational constant (L/T^2), z is the vertical height above a reference datum (L), and k_r is the relative permeability. For fully saturated conditions, as is the case in this paper, Richards' equation reduces to the conventional groundwater flow equation.

Stochastic conductivity field

This study presents a geostatistical numerical simulation approach for the characterization of a stochastic conductivity field. One of the most widely used algorithms for simulating regionalized variables has been sequential Gaussian simulation (SGS) due to the algorithm's simplicity and flexibility (Safikhani et al., 2017). In this study, the hypothetical heterogenous porosity and permeability were realized using an unconditional SGS. Unconditional SGS honors the given estimates overall mean, variance, and correlation lengths which represents the strength and direction of the relationship between variables. SGS is commonly used on gridded coordinate systems and generates realizations of $z(\mathbf{u}_i)$ of a regionalized Gaussian random field at a discrete set of locations $\{\mathbf{u}_1, \ldots, \mathbf{u}_n\}$ by iteratively sampling a value at each location $\mathbf{u}_i$ (Nussbaumer et al., 2018). With a zero-mean random field, SGS can be described as (Nussbaumer et al., 2018):

$$z(\boldsymbol{u}_i) = \sum_{\boldsymbol{j=1}}^{\boldsymbol{i-1}} \lambda_j(\boldsymbol{u}_i)\boldsymbol{z}\left(\boldsymbol{u}_j\right) + \sigma_E(\boldsymbol{u}_i)U_i, \qquad \forall i = 1, \ldots, N \tag{5}$$

where $\lambda_j : j = 1, \ldots, n$ are the kriging weights, σ_E is the kriging standard deviation, and U_i is a value sampled from the standard Gaussian random variable.

Empirical and theoretical equations

Simple methods of estimation to determine a constant apparent or effective dispersivity value have been developed to describe field-scale longitudinal dispersivity as a function of travel distance (Lovanh et al., 2000). A common lumped estimation of dispersivity is based on observations that longitudinal dispersivity values increase with the overall scale or travel distance (Gelhar, 1993). A straight line fit through the origin to estimated values of dispersivity vs. length scale of transport shows a slope of 0.1; thus, the apparent longitudinal dispersivity can be estimated as one tenth the characteristic length of transport:

$$\alpha_L = 0.1 * L \tag{6}$$

where L is the characteristic length of transport (Gelhar, 1993). A secondary method of estimating longitudinal dispersivity characterizes the scale effect of dispersion through fractal analysis excluding data at scales greater than 3500 m (Neuman and Zhang, 1990). The derived empirical relationship for dispersivity is:

$$\alpha_L = 0.0176 * L^{1.46} \quad (7)$$

where L is the characteristic length of transport for scales of L less than or equal to 100 meters (Neuman and Zhang, 1990). For values of L larger than one hundred meters, the longitudinal dispersivity derived empirical relationship is:

$$\alpha_L = 0.32 * L^{0.83} \quad (8)$$

More recent work from Gelhar et al (Gelhar et al., 1992) suggests that longitudinal dispersivity will reach an asymptotic value at large flow regimes with several methods being developed to estimate longitudinal dispersivity from these observations. An empirical relationship that describes this relationship from Xu & Eckstein is:

$$\alpha_L = 0.83(log_{10}(L)^{2.414} \quad (9)$$

where L is the characteristic length of transport (Xu and Eckstein, 1995). This method is used by the Environmental Protection Agency for estimating field-scale values of longitudinal dispersivity (EPA 2013, 2011).

(Schulze-Makuch, 2005) collect dispersivity data from 109 different authors for several types of porous media obtained from laboratory tests, in-field injection tracer tests and plume modeling. From this collection of data, a scaling relationship of longitudinal dispersivity was derived, which includes a factor of the geologic media:

$$\alpha_L = c(L)^m \quad (10)$$

where α_L is the longitudinal dispersivity, c is the mean porosity of the geologic medium, L is the characteristic length of transport, and m is the scaling exponent (Schulze-Makuch, 2005). The assumption of a single value of longitudinal dispersivity based solely on a characteristic transport length adds a source of significant uncertainty as it fails to consider site specific heterogeneity characteristics.

The longitudinal dispersivity in a three-dimensional aquifer can be derived from stochastic analysis of the permeability structure of our simulated heterogenous, statistically anisotropic field where mean groundwater flow is parallel to bedding. For the stratified condition where correlation lengths $\lambda_1, \lambda_2 >> \lambda_3$ where (Gelhar and Axness, 1983):

$$A_{11} \cong \frac{\sigma_f^2 \lambda_1}{\pi^2 \gamma^2} \iiint_{-\infty}^{\infty} \frac{r_* u_3^2 du_1 du_2 du_2}{(r_*^2 u_3^4 + u_1^2)(1 + u^2)^2} \quad (11)$$

$$r_* = \alpha_T \lambda_1 / \lambda_3^2 \quad (12)$$

where α_T is the transverse dispersivity, λ_1 is the correlation length in the mean direction of flow (x direction), λ_2 is the correlation length in the mean direction of flow (y direction), and λ_3 is the correlation length normal to mean direction of flow (z direction). This integral, evaluated asymptotically for small and large values of r_*, yields the equations to calculate our theoretical values of longitudinal dispersivity (Gelhar and Axness, 1983):

$$\alpha_L = \frac{1.311 r_*^{\frac{1}{2}} \sigma_f^2 \sigma_3^2}{\gamma^2 \alpha_T} \quad r_* >> 1 \quad (13)$$

$$\alpha_L = \left(\frac{\sigma^2 * \lambda}{\gamma^2}\right)(1 - r_*) \quad r_* \ll 1 \quad (14)$$

$$\gamma = \frac{q}{K_l * J_l} \quad (15)$$

where r_* is calculated using equation 12, α_T is the transverse dispersivity, σ^2 is the variance of the log-transformed hydraulic conductivity, q is the mean modeled Darcy flux obtained from the synthetic heterogeneous aquifer output file, K_l is the calculated log-transformed hydraulic conductivity, and J_l is the hydraulic gradient defined in our boundary conditions.

Environmental tracers and the flux-averaged concentration equation

Tritium (^3H) is a radioisotope of hydrogen produced in both natural and anthropogenic processes. ^3H concentrations show a distinct peak in their atmospheric concentrations due to hydrogen bomb testing in the 1950's and 1960's (Figure 1), and have been used to characterize groundwater samples with a maximum age of approximately 60 years (Suckow, 2014). Chlorofluorocarbons (CFC-11, CFC-12) and sulfur-hexafluoride (SF_6) are used to date relatively young groundwater (Zuber et al., 2005). CFC production began in the early 1940's with CFC-11 and CFC-12 used mainly for refrigeration and air-conditioning (Kagabu et al., 2017). Production of SF_6 began in the 1950s and was mainly used for its electrical and thermal insulation properties (Chambers et al., 2018). All environmental tracers were introduced into the environment and are subsequently a part of the hydrologic cycle (Chambers et al., 2018). SF_6 atmospheric concentrations are monotonically increasing, while CFC atmospheric concentrations are on the decline since the implementation of the Montreal Protocol first signed in 1987 (Figure 1). Atmospheric concentrations over time for all environmental tracers for both the northern and southern hemispheres are readily available for public use through the National Oceanic and Atmospheric Administration (NOAA).

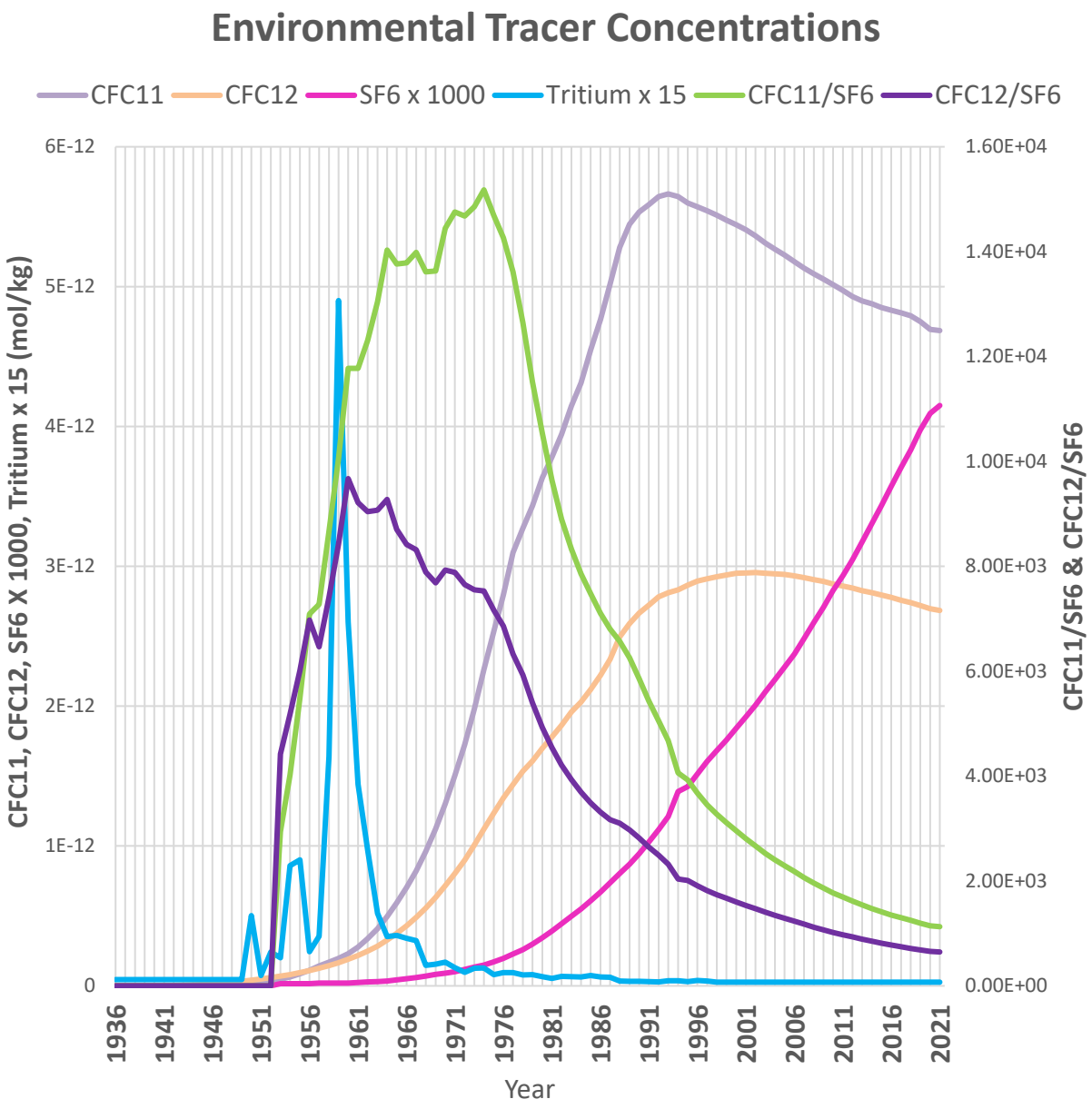

Figure 1 – Atmospheric concentrations of CFCs, SF_6, Tritium, CFC11/SF_6 and CFC12/SF_6 from 1936 to 2021.

We calculated the flux-averaged concentration for the environmental tracers CFC11, CFC12, SF_6, tritium, and the ratios of CFC11/SF_6 and CFC12/SF_6 as our observational datasets for inversion modeling. Flux-averaged concentration quantifies the solute mass crossing a surface within a specified time interval normalized by the velocity field (Shapiro and Cvetkovic, 1988):

$$\overline{C_f} = \frac{\oiint C * (q \cdot n) dS}{\oiint (q \cdot n) dS}$$

where q is the Darcy flux, n is the vector normal to the surface, and C is the resident concentration. We calculate C_f in our numerical model as:

$$\overline{C_f} = \frac{\sum_i (C_i * Q_i)}{\sum_i Q_i} \quad (16)$$

where C_i is the concentration of the i_{th} cell along the plane and Q_i is the discharge normal to the plane of the i_{th} cell.

4. Methods

Conceptual model

Synthetic aquifers allow us to control errors in observations, all boundary conditions, domain geometry and groundwater velocity. Simplified synthetic aquifers allow us to mimic typical in-field groundwater system studies where a simplified representation of an aquifer, which lacks the full description of the true heterogeneous permeability distribution, is calibrated based on a limited number of site observations. A 3D heterogenous synthetic confined aquifer with dimensions of 100m x 100m x 10m, was gridded at 1m x 1m x 1m. No-flow boundaries were applied on the top and bottom with groundwater flow from east to west, and a head gradient set to 0.01 m/m on the west and east boundaries. A fully screened well over the full length of the z direction, 10 m (Figure 3), was placed at the center at 50 m in the x direction and 50 m in the y direction.

A 3D homogeneous synthetic confined aquifer used in model calibration was developed with dimensions of 100m x 100m x 10m, gridded with 1m x 1m x 1m grid blocks. Boundary conditions for this homogeneous model are identical to the 3D heterogeneous model. This simplified 3D model was used for model calibration.

Historic atmospheric CFC11, CFC12, SF_6 and ^3H concentrations from 1940 to 2021 were obtained from NOAA ("NOAA Global Monitoring Laboratory - Halocarbons and other Atmospheric Trace Species") and aqueous phase concentrations were calculated using Henry's Law at a temperature of 25 °C, 1 atm of pressure, and no addition of excess air (Aeschbach-Hertig et al., 2000). A zero gradient transport boundary condition only allows advective solute flux out of the domain, was applied to the eastern discharge boundary. No mass transport conditions were assigned to the remaining boundaries. These concentrations were applied to the western boundary in groundwater flow and were assumed to be non-sorbing and chemically inert, which is reasonable for these tracers (Cook, 2000).

Heterogeneity modeling – sequential Gaussian simulation

Geostatistical simulation was used to develop the 3D heterogeneous, stochastic porosity and permeability fields. Sequential Gaussian simulation (SGSIM) was implemented using the open-sourced software SGSIM functionality from the Geostatistical Software Library, GSLIB, software package. Porosity is a key control on the permeability due to larger pores resulting in larger pathways for groundwater fluids to travel through. The unconditional 3D heterogeneous porosity field was developed using a mean porosity of 0.18, a standard deviation of 0.05 and a correlation length of 10 m in the x direction, 10 m in the y direction, and 5 m in the z direction. The 3D heterogeneous permeability truth field was developed conditionally from the porosity field using a log-normal permeability distribution with a mean of 10^{-13} m^2, one order of standard deviation and a correlation length of 10 m in the x direction, 10 m in the y direction, and 5 m in the z direction. To verify a positive correlation between porosity and permeability we performed least squares regression between the two parameters, calculated their R^2 value and developed a scatterplot to visualize the linear relationship.

Groundwater flow and transport modeling

Steady-state groundwater flow and transient transport of all concentrations through synthetic aquifers were conducted using the PFLOTRAN reactive transport software (Hammond et al., 2012; Gardner et al., 2015). The PFLOTRAN software is a scalable, parallel, multiphase, multicomponent, non-isothermal reactive flow and transport code that solves the advection-dispersion equation using fully implicit, integral finite technique (Hammond et al., 2012). PFLOTRAN was run in Richards' mode solving for single-phase variably saturated groundwater flow and mass transport using the advection-dispersion (eq. 2) and Richards' equations (eq.4). For all synthetic heterogeneous models, longitudinal and transverse dispersivity were set to zero. Key parameter values used in the synthetic aquifer simulation are presented in Table 1.

Table 1. Table of model parameters for the heterogeneous and homogeneous synthetic aquifers.

Parameter	**Value**	**Unit**	**Description**
$^{3}H_{t\,½}$	12.3287	year	Tritium half-life
k	10^{-13}	m^2	Mean Permeability
n	0.18	-	Mean Porosity
ω	0.5	-	Tortuosity
D_m	10^{-9}	-	Molecular Diffusion Coefficient

Simulations of the environmental tracers through the heterogenous aquifer were performed in two steps. 1) To generate initial conditions, constant concentration boundary conditions of pre-anthropogenic environmental tracer concentrations were applied to the west boundary for 10^6 years to reach steady state. 2) The steady state model was then restarted and the historical, anthropogenic environmental tracer concentrations over a period of one hundred years were applied to the west boundary. The decay constant for ^{3}H

was set to 12.3287 years, and the subsurface production of both ^{3}H and SF_6 was neglected for this study (Cook, 2000).

Calibration data

Environmental tracer concentrations used in the calibration datasets were generated from a PFLOTRAN forward model run parameterized with the 3D synthetic heterogenous permeability field. The environmental tracers CFC11, CFC12, SF_6 and ^{3}H were determined from a fully screened well located at the center of the heterogenous synthetic aquifer running the full z direction (10 m) of the 3D model. The transient environmental tracer concentrations were simulated throughout the full numerical domain with a full simulation time of one hundred years. Flux-averaged concentrations were calculated (eq. 16) for the individual tracers and the ratios of CFC11 and CFC12 over SF_6.

Model calibration

Automated model calibration was used to estimate best-fit longitudinal dispersivity values for the homogeneous model constrained to the different environmental tracer flux-averaged concentration observation datasets. Flux-averaged concentrations of the individual environmental tracers, including the ratios of CFCs/SF_6, were used to perform independent model calibrations of longitudinal dispersivity for two time series. The first time series represented samples obtained from the full run of one hundred years. The second time series was a single flux-averaged concentration series representative of 2021. The observation dataset was directly compared to the simplified model simulation results.

Model calibrations were implemented using the open source Parameter Estimation software (PEST) package (Doherty and Hunt, 2010). The objective of PEST and inverse modeling was to find the optimal set of parameters that provides the minimum value of the weighted least-squares residual objective function. PEST considered longitudinal dispersivity ranging from 0.001 m to 110 m to find the best parameter set that represents the physical behavior of the truth model. Observation datasets required a choice of observation weights, which is an inherently subjective process (Doherty, 2007) ,which

controls the contribution of the observation to the objective function. Here, a constant weight of 1 was assigned to all observations in the dataset so that no single observation dominated the objective function and that all flux-averaged environmental tracer concentrations in the observation datasets imparted equal influence on the calibration (Doherty, 2007). Tracer-derived longitudinal dispersivity values for the full time series were reported along with the 95% confidence interval, where the single time series only reports a single derived value.

TEST – Synthetic contaminant with new boundary conditions

We assess the ability of tracer-derived longitudinal dispersivity to predict independent contaminant transport by simulating transport of a synthetic contaminant through the heterogeneous 3D synthetic flow field with two different inlet boundary conditions: a pulse inlet boundary condition and step-function boundary condition. Both boundary conditions were applied at the west boundary of the steady state heterogenous synthetic aquifer.

A pulse input of the synthetic contaminant represents a boundary condition where a mass of the chemical was added instantaneously at x = 0 with a short injection time. The initial contaminant concentration was set to zero at time t = 0. This pulse injection was analogous to the injection of tritium in our aquifer system. The pulse boundary condition is (Singh et al., 2011):

$$c(x,t) = 0; x \geq x_0, t = 0$$

$$c(x,t) = \begin{cases} c_o;\ 0 < t <\ t_0\,, & x =\ x_0 \\ 0;\ t >\ t_0, & x =\ x_0 \end{cases}$$

A step-function input of the synthetic contaminant assumes that the concentration in the synthetic aquifer prior to the introduction of the solute is zero. The step-function injection of the contaminant is more like the long-term addition of CFCs and SF_6 in our aquifer system. The boundary conditions represented by the step-function are (Correa, 1988):

$$c(x,0) = 0 \quad x \geq 0$$

$$c(0,t) = c_0 \quad t \geq 0$$

$$c(\infty,t) = 0 \quad t \geq 0$$

We varied the values of longitudinal dispersivity in our homogenous models using the values calculated from the theoretical equation (eq. 12 & 14), empirical equations (eq. 6-10), and the optimized values obtained from the PEST model calibrations from both the full-time and single-time series. We calculated the flux-averaged concentrations (eq. 16) of the synthetic contaminant from the same fully screened well located at the center of the heterogeneous and homogeneous aquifers.

Breakthrough curves, misfit plots, and Pearson's Chi-squared goodness of fit test

We evaluate the ability of our 3D homogeneous model with tracer-derived, empirical, and theoretical longitudinal dispersivity values to fit the synthetic contaminant breakthrough curves of concentration over time using breakthrough curve matching and misfit plots. Here we match breakthrough curves of the flux-averaged concentration, and the time of arrival at our fully screened well (Li, 2011).

We simulated breakthrough curves for both the step and pulse contaminant flux-averaged concentrations for the truth model and all values of empirically, theoretically, and tracer-derived (full-time and single-time series) longitudinal dispersivity. We then calculated the residual misfit and plotted a data misfit scatter plot of the value of dispersivity on the x axis and misfit value on the y axis to evaluate which values of longitudinal dispersivity best fit the true observation dataset. The following equation was used to calculate the misfit for all models:

$$e = \sum_{i=1}^{n} (y_i - \hat{y}_i)^2 \qquad (17)$$

where e is the misfit, y_i is the observed model value and $\widehat{\hat{y}_i}$ is the i^{th} predicted model value.

We used Pearson's Chi-squared goodness of fit test to assess how well the observed data fit correspond to the observed (truth) model. The chi-squared goodness of fit test was designed for the following hypothesis:

H_0: The observed model fits the expected model; there is no significant difference between the observed and expected values.

H_a: The observed model does not fit the expected model; there is a significant difference between the observed and expected values.

The following equation was used to calculate the chi-squared value for all time points:

$$\chi^2 = \sum_{i=1}^{k} \frac{(O_i - E_i)^2}{E_i} \quad (18)$$

where O_i is the observed value and E_i is the expected value for all time points. The chi-squared test statistic follows a chi-square distribution with $(k - c)$ degrees of freedom where k is the number of values in each array and c is the number of parameters for the distribution + 1. The null hypothesis is rejected if:

$$\chi^2 > \chi^2_{1-\alpha,k-c} \quad (19)$$

where $\chi^2_{1-\alpha,k-c}$ is the chi-squared critical value with $k - c$ degrees of freedom and significance level α. For this study α was set to 0.05, k was determined from the number of flux-averaged values in each array and c was set to 2. We calculated the chi-squared values for all models and compared the calculated chi-squared values to the chi-squared critical values. If the test statistic was lower than the critical value, we fail to reject the null hypothesis that the observed models fit the expected model. If the test statistic was higher than the critical value, we rejected the null hypothesis and determined that the observed models did not fit the expected model.

5. Results

Heterogeneous 3D Synthetic Aquifer

A histogram of the log permeability values from the SGS for the 3D heterogeneous model is given in Figure 2. The distribution of log permeability values is unimodal, which confirms a Gaussian distribution, centered at a median of 10^{-13} m, with values ranging from 10^{-13} to 10^{-9}, and a standard deviation of one. A histogram from the SGS simulation for the porosity values (Figure 2) displays a Gaussian distribution with a slight right-hand skew. The values of porosity are centered at the median of 0.18, with values ranging from 0.1 to 0.28 with an interquartile range of 0.02 (Figure 3).

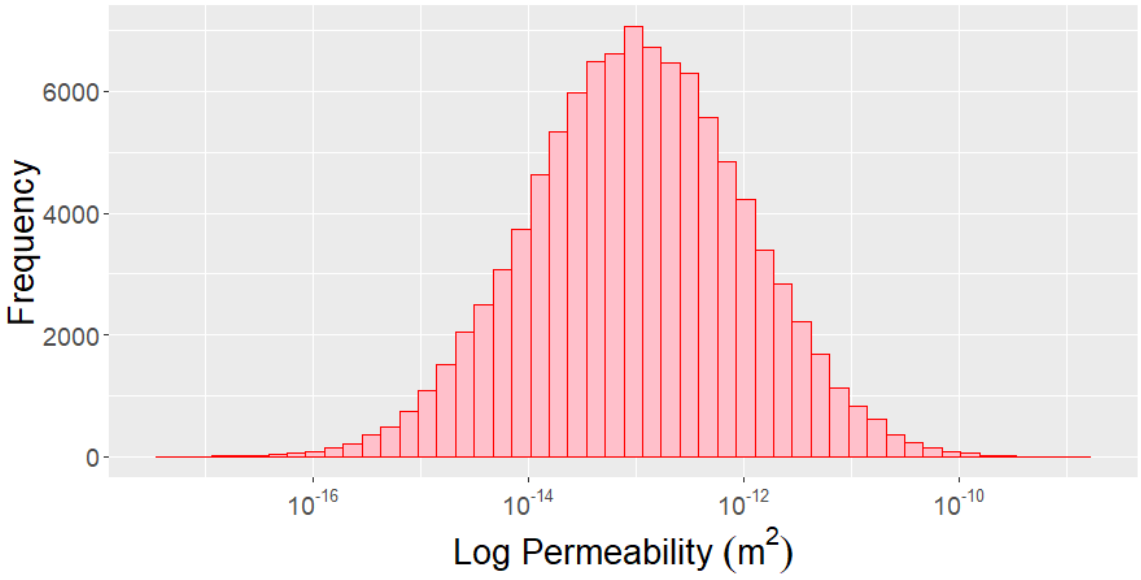

Figure 2 – Histogram of the log permeability values from the 3D heterogeneous synthetic aquifer.

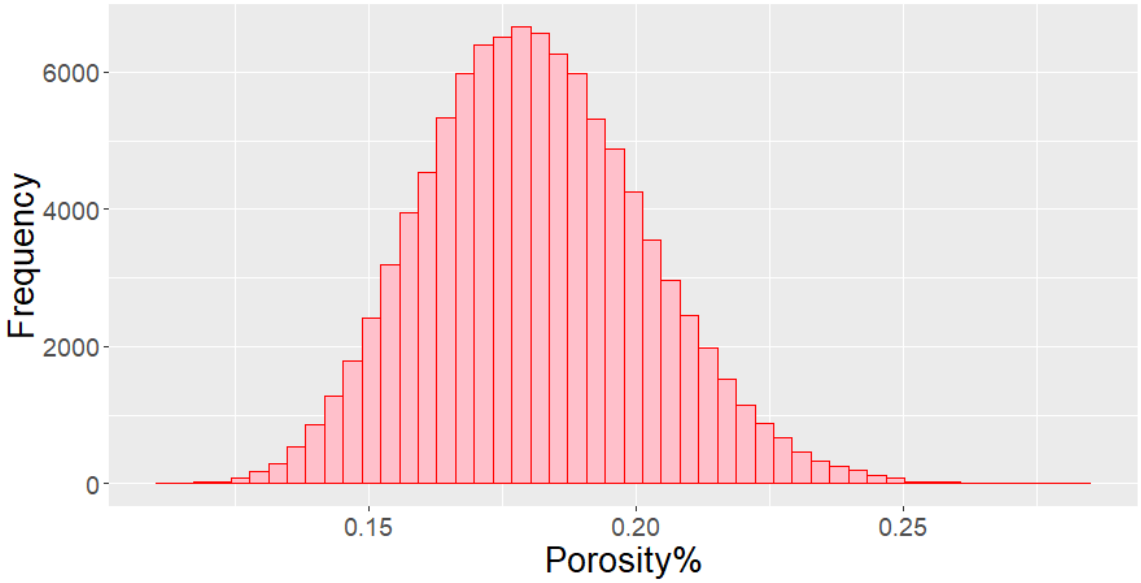

Figure 4 – Histogram of the porosity values from the 3D heterogeneous synthetic aquifer.

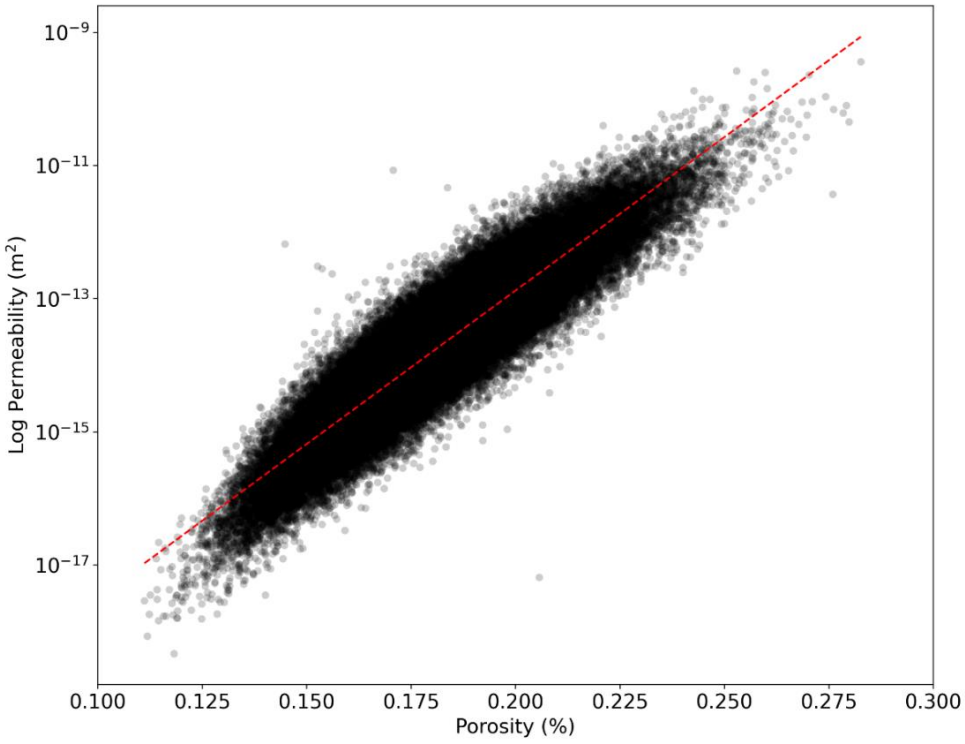

Figure 3 – Scatter plot of porosity on a linear scale against permeability on a logarithmic scale with a least squares' regression line.

Figure 4 is a scatter plot of the simulated porosity values compared to the simulated log permeability. Log permeability was correlated with porosity; as the porosity increased, the permeability also increased showing a strong linear relationship ($R^2 = 0.83$).

A visualization of the 3D heterogeneous synthetic aquifer (Figure 5) shows the true permeability distribution on a log scale. The values of permeability range from 3.9×10^{-19} to 1.3×10^{-9} m^2. The figure also displays the simulated location of the fully screened well used to extract all flux-averaged concentrations.

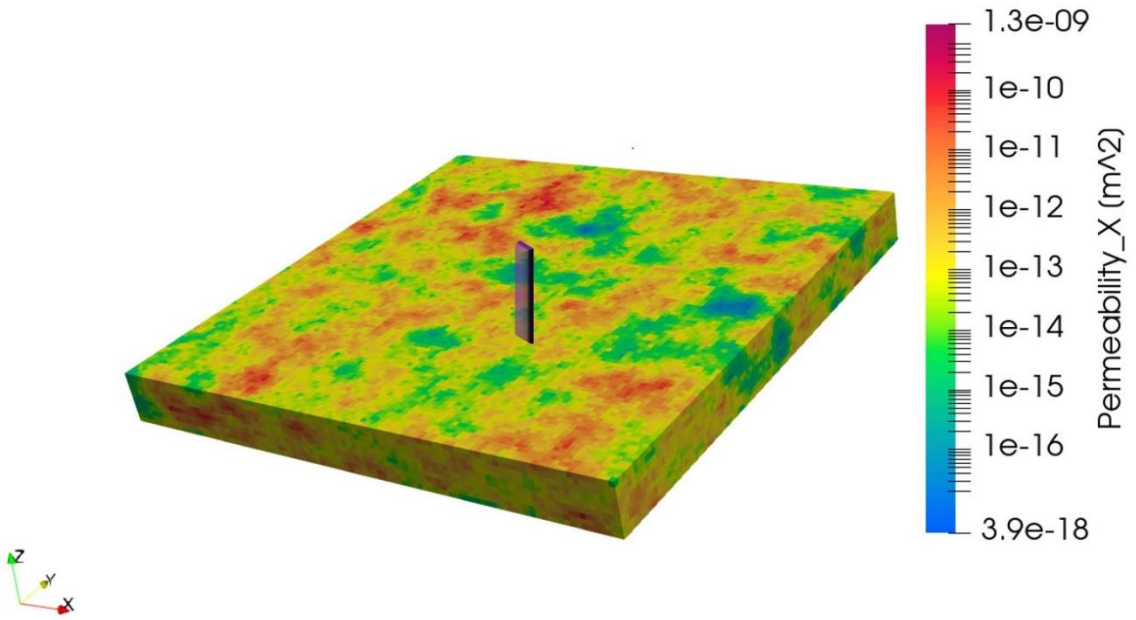

Figure 5 – True permeability field for the 3D synthetic aquifer model created using SGS and a log-normally distributed prior. Figure shows a simulation of the fully screened well at the center of the synthetic field running the full z direction of 10 m.

Theoretical and Empirically Derived Longitudinal Dispersivity

The theoretical longitudinal dispersivity value of 3.19 m was calculated using equations 12 and 14. The value of the variance of the log transformed hydraulic conductivity was 1, the correlation length in the mean direction of flow in the x direction was 10 m, the average modeled Darcy flux from the steady-state heterogeneous aquifer was 0.62 m/yr, and the calculated Darcy flux from the log-transformed hydraulic conductivity and hydraulic gradient was 0.35 m/yr. The empirical values of longitudinal dispersivity were calculated from equations 6, 7, 9, and 10. A length value, L, of 50 m was

used in these equations corresponding to the location of the fully screened well in the synthetic aquifer in the x direction. The five different calculations estimated the value of dispersivity to be anywhere from 1.01 m to 5.32 m.

Table 2 – Empirically and theoretically derived values of longitudinal dispersivity with their respective equations.

Theoretical & Empirical Dispersivity	**Calculation – 50m length**	**Dispersivity (meters)**
Gelhar, 1993	$\alpha_L = 0.1 * L$	5.00
Neuman & Zhang, 1990	$\alpha_L = 0.0176 * L^{1.46}$	5.32
Xu & Eckstein, 1995	$\alpha_L = 0.83\left(log_{10}(L)\right)^{2.414}$	2.98
Schulze-Makuch, 2005	$\alpha_L = 0.18(L)^{1.46}$	1.01
Gelhar & Axness, 1983 (Theoretical)	$\alpha_L = \frac{\sigma^2 * \lambda}{\gamma^2}$	3.19

Table 3 shows the values of longitudinal dispersivity, and their 95% confidence intervals, derived from PEST optimizations from the full time series from a single, specified, environmental tracer and the ratios of CFC11/SF_6 and CFC12/SF_6. The tracer-derived values from the full-time series optimizations are between 2.03 m to 4.38 m with SF_6 having the lowest and CFC11 having the highest, respectively. We observe that the tracer-derived value from tritium at 4.19 m is slightly higher than the derived values for CFC11/SF_6 and CFC12/SF_6 at 4.12 and 4.10, respectively

Table 3 – Full-time series tracer-derived values of longitudinal dispersivity from PEST inversions.

Tracer - Full Time Series	**Optimization Results - Dispersivity (meters)**	**95% CI lower limit**	**95% CI upper limit**
CFC11	4.38	3.47	5.28
CFC12	3.58	2.61	4.54

^{3}H	4.19	3.70	4.68
SF_6	2.03	1.79	2.27
CFC11/SF_6	4.11525	4.00	4.24
CFC12/SF_6	4.08558	3.91	4.26

Tracer-derived values of longitudinal dispersivity optimized from a single-time concentration dataset representative of 2021 are shown in Table 4. The 95% confidence intervals are not applicable from a single observation dataset PEST inversion. Tracer-derived values of longitudinal dispersivity are between 1.96 m to 10.75 m with the lowest and highest values being derived from the SF_6 and CFC11 concentrations, respectively.

Table 4 – Single-time series (2021) tracer-derived values of longitudinal dispersivity from PEST inversions.

Tracer - Single Time Series, 2021	**Optimization Results - Dispersivity (meters)**
CFC11	10.75
CFC12	7.26
^{3}H	5.89
SF_6	1.96
CFC11/SF_6	4.42
CFC12/SF_6	4.37

The clustered bar graph in Figure 6 displays the calculated and optimized values of longitudinal dispersivity. The full-time series and single-time series tracer-derived values are in red and blue, respectively. The theoretical and empirically derived values are in yellow and green, respectively. Values of longitudinal dispersivity derived from theoretical and empirical calculations are estimated to be from 1.01 m to 5.32 m. Tracer-derived values from the full time series are between 2.03 m to 4.38 m, and the tracer-derived values from the 2021 time series are between 1.96 m to 10.75 m.

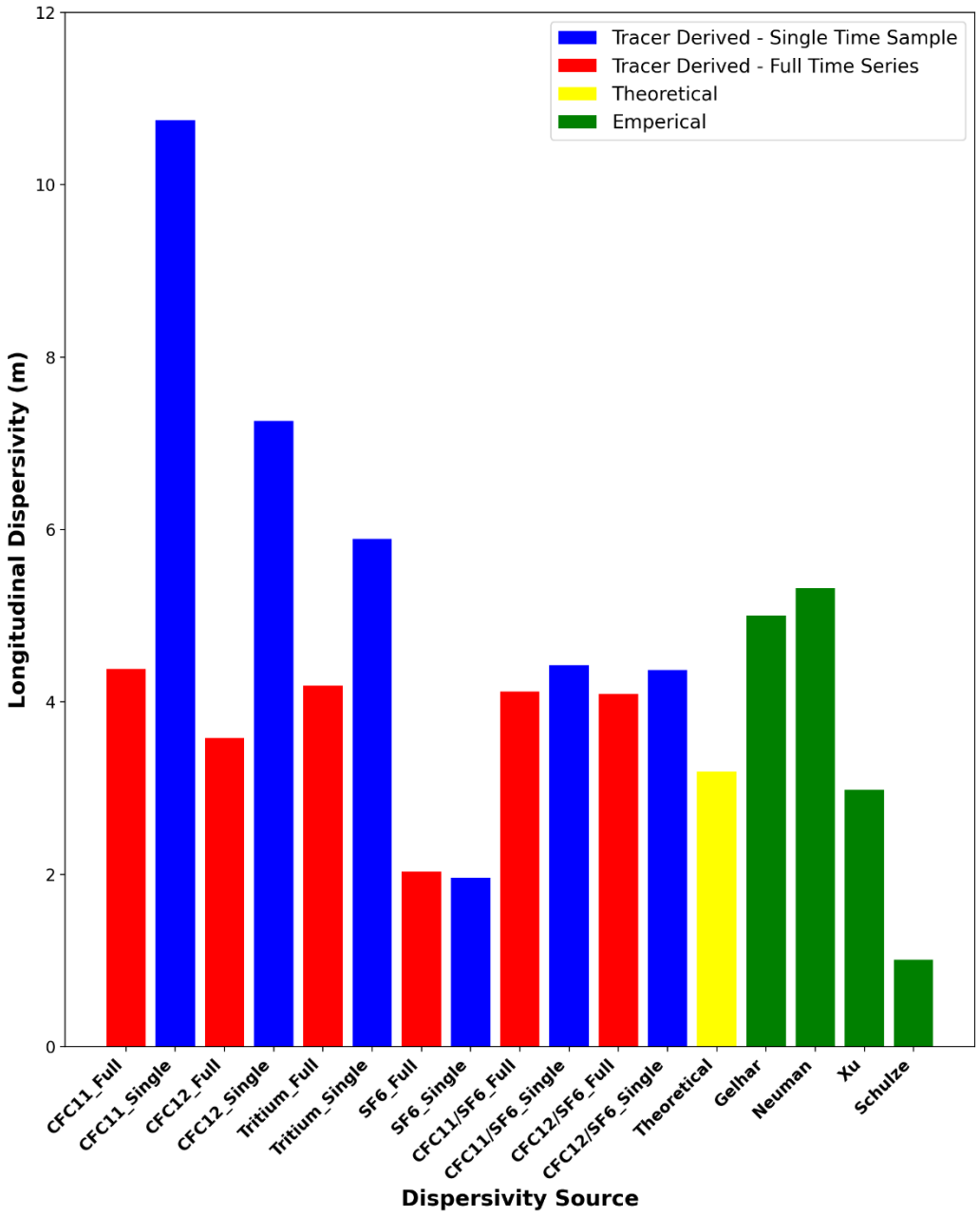

Figure 6 – Clustered bar graph of longitudinal dispersivity values with their respective sources.

Analysis of step function boundary condition breakthrough curves, misfit plots, and χ^2

The breakthrough curves for values of dispersivity derived from theoretical and empirical calculations are shown in Figure 7. We observe the models with dispersivity from Gelhar and Neuman & Zhang overlap each other throughout the plot with an arrival time of 5 years and the curves consistently sit just above the truth model. The model with dispersivity from Xu & Eckstein and the theoretical calculation overlap each other throughout the figure with an arrival time later than the truth model around 8 years. These curves follow the truth model until the 25-year mark where the concentrations increased above the truth model and remain higher throughout. The Schulze-Makuch model displays the latest arrival time around 9 years. This curve intersects the truth model at about the 25-year mark. At around 40 years, this curve increased above all other curves and displays a maximum concentration at approximately 65 years.

Figure 8 displays the breakthrough curves modeled using longitudinal dispersivity values derived from the full time-series. All breakthrough curves, excluding SF_6, display an initial arrival time of the synthetic contaminant at around 5 years. These plots overlap throughout following the truth model until about approximately 15 years where concentrations remain consistently above the truth model. The SF_6-derived model initial concentration arrives at the 9-year mark. These concentrations remain below the truth model until approximately 22 years where it then intersects the truth model and continues to steadily increase above all models with a maximum concentration at approximately 75 years.

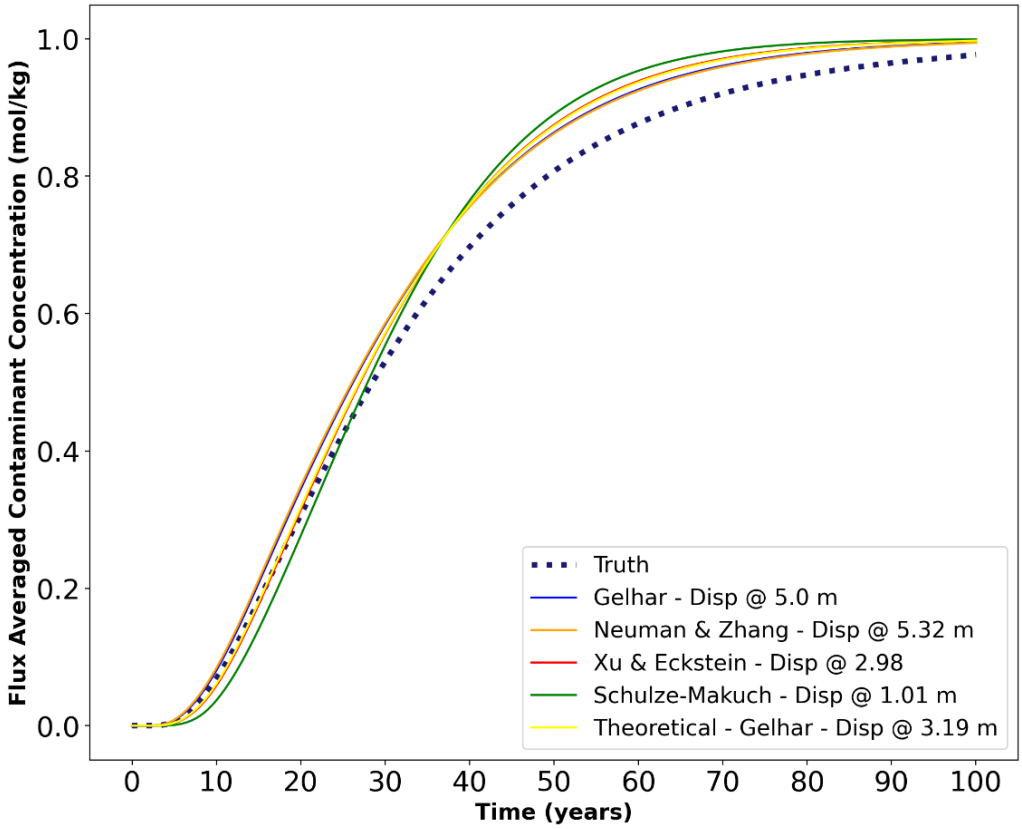

Figure 7 – Breakthrough curves for the step function inlet boundary condition displays the flux-averaged contaminant concentration for the synthetic contaminant on the y-axis and time in years on the x-axis. Curves represent the heterogeneous truth model (dark blue dashed line) and the models with values of longitudinal dispersivity from the theoretical or empirically derived calculations.

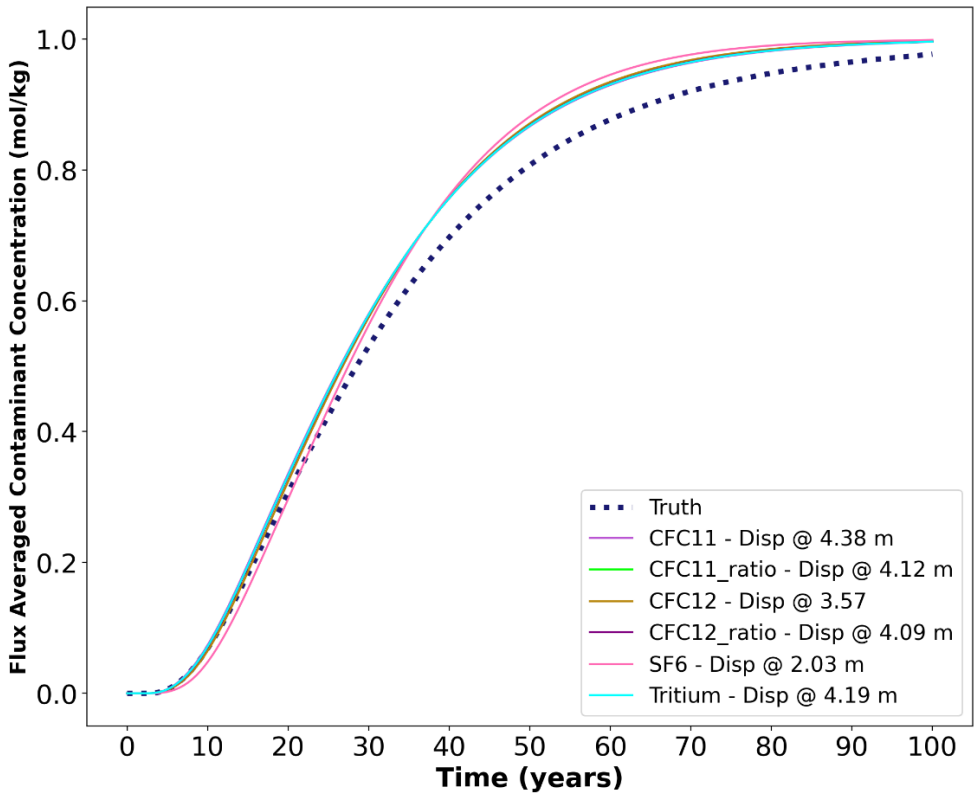

Figure 8 - Breakthrough curves for the step function inlet boundary condition displays the flux-averaged contaminant concentration for the synthetic contaminant on the y-axis and time in years on the x-axis. Curves represent the heterogeneous truth model (dark blue dashed line) models with values of longitudinal dispersivity derived from the full-time series.

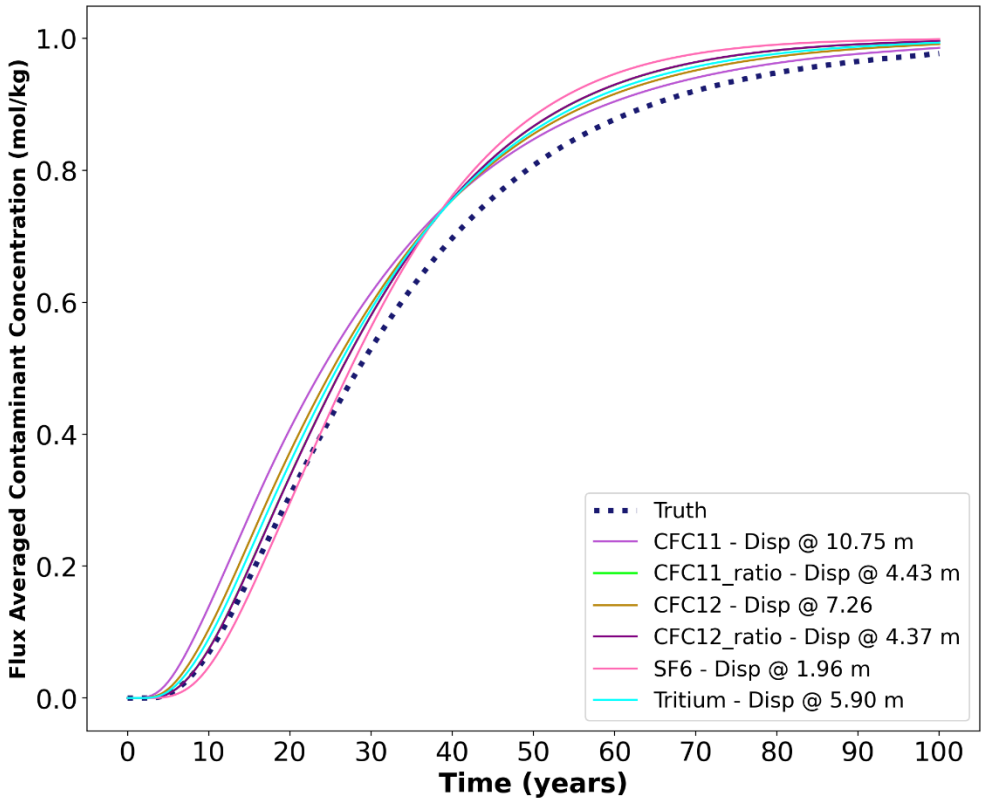

Figure 9 - Breakthrough curves for the step function inlet boundary condition displays the flux-averaged contaminant concentration for the synthetic contaminant on the y-axis and time in years on the x-axis. Curves represent the heterogeneous truth model (dark blue dashed line) and models with values of longitudinal dispersivity derived from a single-time series representative of 2021.

The breakthrough curves for values derived from the single-time series are shown in Figure 9. We observe the first concentration arrival from the CFC11 tracer-derived value at 3 years with the concentrations above the truth model throughout, and a maximum concentration at approximately 62 years. The concentrations from the CFC12-derived model remain consistently higher than the truth model with an initial breakthrough at approximately 5 years and a maximum concentration of approximately 80 years. The SF_6-

derived model displays an arrival time at the 9-year mark and remains lower than the truth model until the 20-year mark where the concentrations match the truth model briefly before they increase above all other models at about 40-years. CFC11/SF_6, and CFC12/SF_6 derived modeled concentrations overlap each other throughout the plot with an approximate arrival time at 8 years. We observe these ratio-derived models to sit just above the truth model where at approximately 15 years the concentrations diverge above the truth model with a maximum concentration around 75 years. The tritium-derived model follows above the ratio-derived models throughout the plot. At approximately 38 years, this model intersects the ratio-derived models where concentrations remain lower than the ratio-derived models and display a maximum concentration around 80 years.

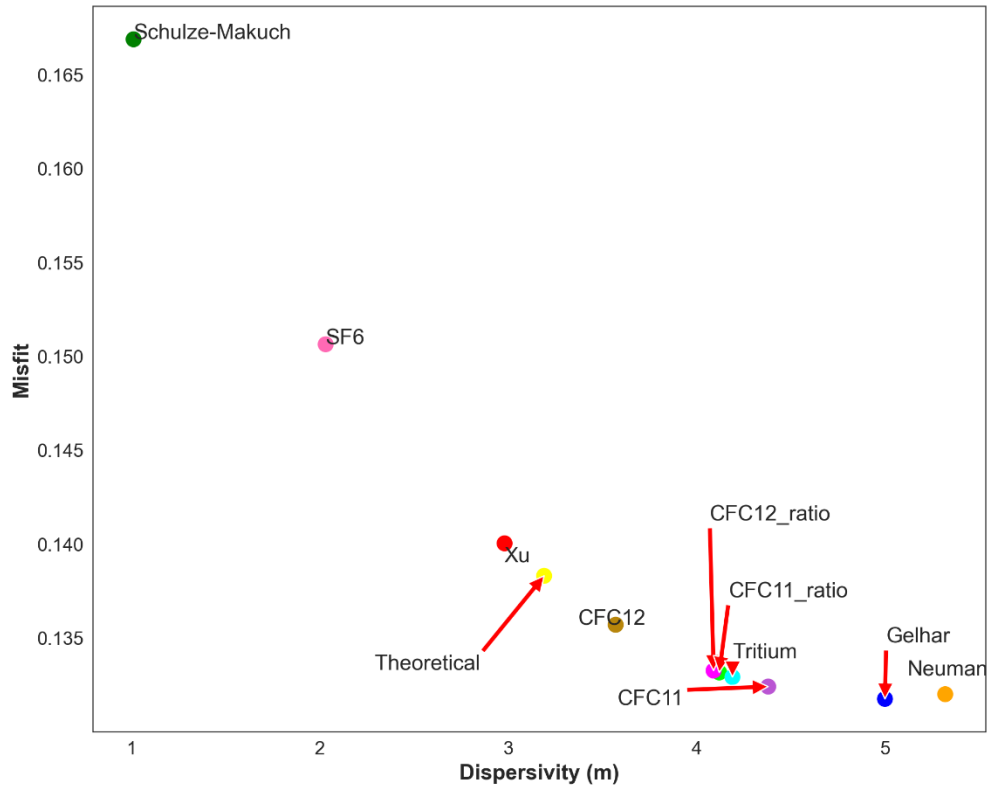

Figure 10 – Step function, full-time series misfit plot displaying the misfit value on the y-axis and the tracer-derived, theoretical, and empirical values of longitudinal dispersivity (m) on the x-axis.

The misfit plot in figure 10 addresses the misfit quantification of the residuals for dispersivity values estimated using the full time series. The largest misfit was from Schulze-Makuch with a misfit of 0.167. There is no large statistical difference in the misfit values for the CFC12 ratio, CFC11 ratio, tritium, and the empirically calculated values from Gelhar and Neuman. All misfit values from these sources of dispersivity are between 0.130 and 0.135.

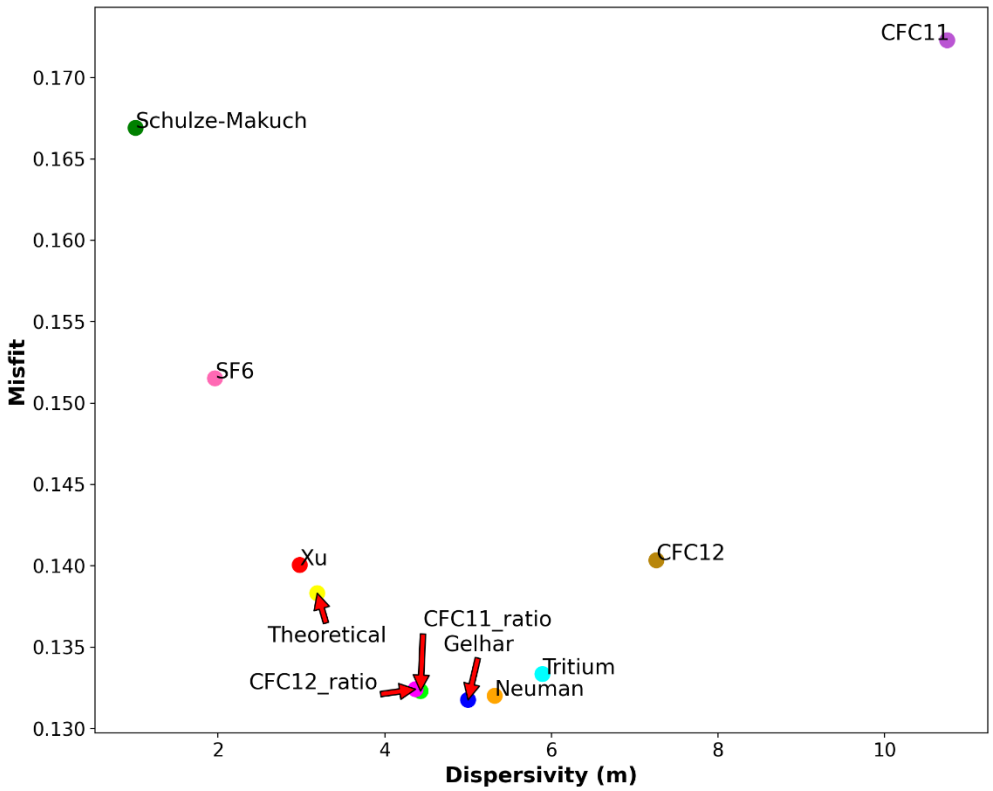

Figure 11 – Step function, single-time series misfit plot displaying the misfit value on the y-axis and the tracer-derived, theoretical, and empirical values of longitudinal dispersivity (m) on the x-axis.

The misfit plot in figure 11 addresses the misfit quantification for dispersivity values estimated using the single time series. The largest misfit was for dispersivity from CFC11 with a misfit of 0.172, and Schulze-Makuch with a misfit of 0.167. We again see that the best-fit misfit values between 0.130 and 0.135 come from the tracer-derived values of dispersivity for the CFC11 ratio, CFC12 ratio, tritium, Neuman and Gelhar.

Table 5 – Step function, full-time series chi-squared goodness of fit values.

Longitudinal Dispersivity Source	χ^2
Theoretical Calculation - 3.19 m	2.6×10^{-2}
Gelhar - 5.0 m	2.9×10^{-2}
Neuman & Zhang - 5.32 m	3.2×10^{-2}
Xu & Eckstein - 2.98 m	2.7×10^{-2}
Schulze-Makuch - 1.01m	5.4×10^{-2}
CFC11, Full Time Series - 4.38 m	2.5×10^{-2}
CFC12, Full Time Series - 3.57 m	2.5×10^{-2}
Tritium, Full Time Series - 4.19 m	2.5×10^{-2}
SF_6' Full Time Series - 2.03 m	3.7×10^{-2}
CFC11 ratio, Full Time Series - 4.12 m	2.5×10^{-2}
CFC12 ratio, Full Time Series - 4.09m	2.4×10^{-2}

Table 5 displays the values of the chi-squared goodness of fit test (equations 18 & 19) to determine how well the observed models for values dispersivity derived from the full-time series, and theoretical and empirically derived values, fit our observed truth model. The critical chi-squared value is 44.99 with 31 degrees of freedom. The chi-squared test statistic for all models fails to reject the null hypothesis, and there is no significant difference between each of the observed models.

Table 6 - Step function, single-time series chi-squared goodness of fit values.

Longitudinal Dispersivity Source	χ^2
Theoretical Calculation - 3.19 m	2.6×10^{-2}
Gelhar - 5.0 m	2.9×10^{-2}
Neuman & Zhang - 5.32 m	3.2×10^{-2}
Xu & Eckstein - 2.98 m	2.7×10^{-2}
Schulze-Makuch - 1.01m	5.4×10^{-2}
CFC11, Single Time Series - 10.75 m	2.3×10^{-1}
CFC12, Single Time Series - 7.26 m	6.7×10^{-2}
Tritium, Single Time Series - 5.89 m	3.9×10^{-2}
SF_6, Single Time Series - 1.96 m	3.7×10^{-2}
CFC11 ratio, Single Time Series - 4.43 m	2.5×10^{-2}
CFC12 ratio, Single Time Series - 4.37 m	2.5×10^{-2}

Table 6 displays the values of the chi-squared goodness of fit test (equations 18 & 19) to determine how well the observed models for values dispersivity derived from the single-time series, and theoretical and empirically derived values, fit our observed truth model. The critical chi-squared value is 44.99 with 31 degrees of freedom. The chi-square test statistic for all observed models fails to reject the null hypothesis, and there is no significant difference between individual observed models.

Analysis of pulse input boundary condition breakthrough curves and misfit plots

The breakthrough curves from the theoretical and empirically derived values are shown in Figure 12. Breakthrough curves with dispersivity derived from Gelhar and Neuman & Zhang overlap continuously and display an initial arrival time congruent with the truth model around 5 years. These models followed above the truth model until about the 47-year mark, where they cross and dip below the truth model. Models with dispersivity values from Xu & Eckstein and the theoretical calculation overlap throughout the plot with an arrival time around 15 years and a peak concentration around 25-years. At the 55-year

mark they decline below the truth model where they remain. The model with dispersivity from Schulze-Makuch displays the slowest arrival time at about 8 years but displays the largest concentration peak at about 30 years.

The breakthrough curves from the full-time series of tracer-derived values are shown in Figure 13. Excluding SF_6, all models initially follow the truth model with the contaminant arrival time around 4 years. We observe these models overlapping throughout the plot, diverge from the truth model around 12 years and display a peak concentration approaching 25 years. The plots continue above the truth model until around the 52-year mark where they dip and persist beneath the truth model. The SF_6 tracer-derived model shows a delayed arrival time after the truth model at around 7 years. Concentrations remain below the truth model until around the 17-year mark where they rapidly increased above the truth model followed by a concentration peak at around 30 years. Concentrations remain above the truth model until it converges with the truth model around 57 years.

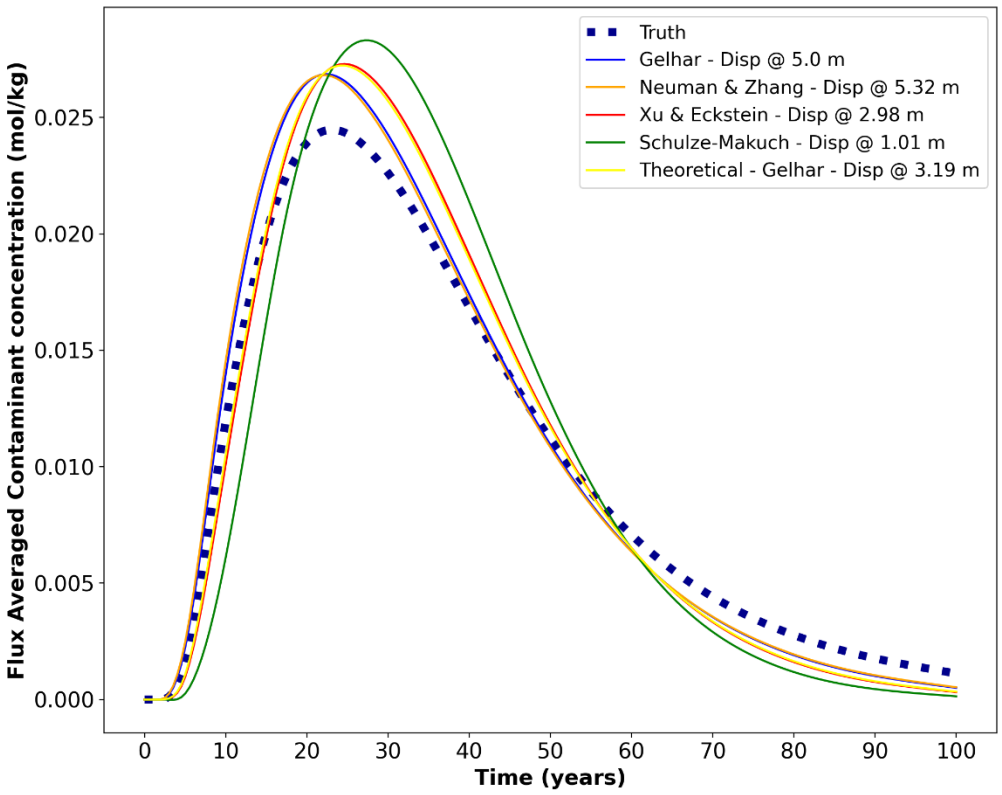

Figure 12 - Breakthrough curves for the pulse inlet boundary condition. Curves represent the heterogeneous truth model (dark blue dashed line) and the simplified homogenous models using values of longitudinal dispersivity derived from theoretical and empirical calculations. The top righthand legend displays the tracer-derived source, value of longitudinal dispersivity in meters, and their associated color in the plot.

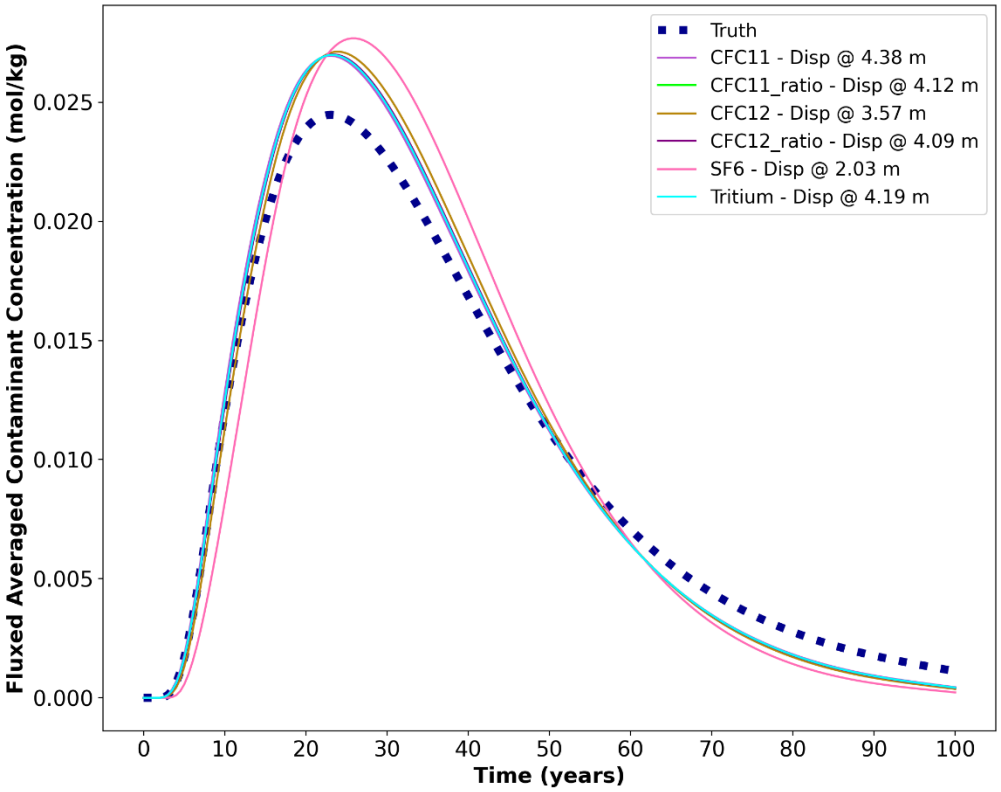

Figure 13- Breakthrough curves for the pulse inlet boundary condition displays the flux-averaged contaminant concentration for the synthetic contaminant on the y-axis and time in years on the x-axis. Curves represent the heterogeneous truth model (dark blue dashed line) and the models using values of longitudinal dispersivity derived from the full-time series.

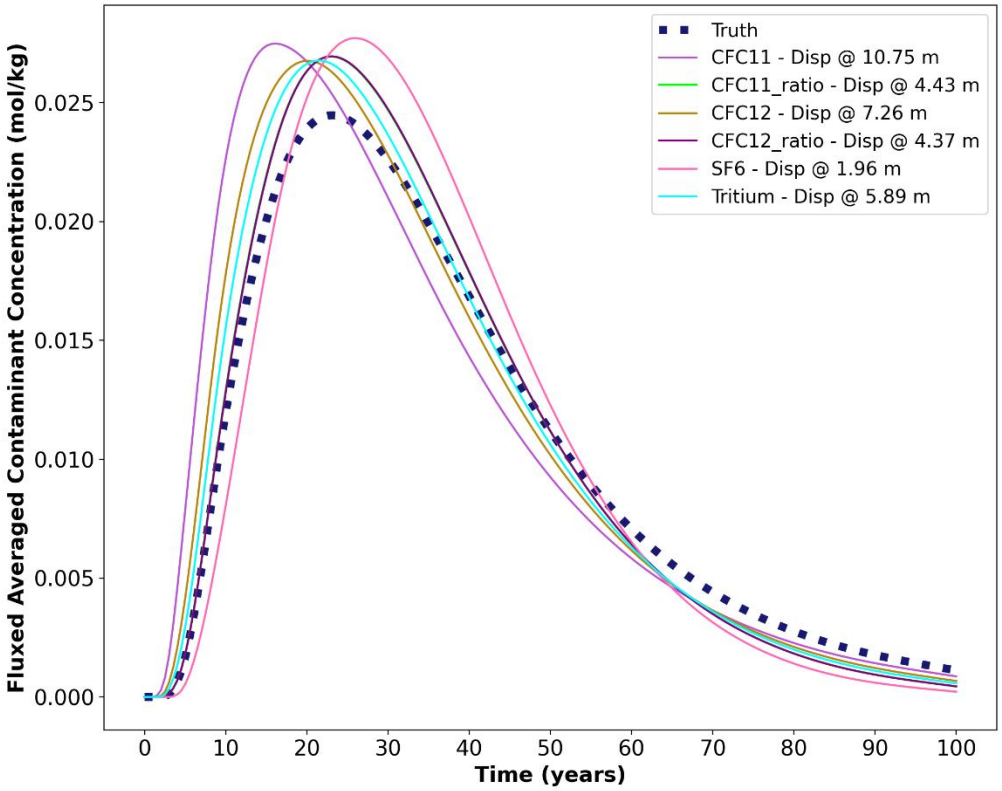

Figure 14- Breakthrough curves for the pulse inlet boundary condition displays the flux-averaged contaminant concentration for the synthetic contaminant on the y-axis and time in years on the x-axis. Curves represent the heterogeneous truth model (dark blue dashed line) and models using values of longitudinal dispersivity derived from the single-time series representative of 2021.

The breakthrough curves for the 2021-time series of tracer-derived values are shown in Figure 14. We observe the first arrival time of the contaminant around 2 years from the model with dispersivity derived from CFC11 with a peak concentration at around 13 years. The CFC11 derived model crossed the truth model around the 30-year mark. The CFC12 derived curve displays the second arrival of the synthetic contaminant around 4 years with a peak concentration at around 25 years and intersects with the truth model around 37 years. The SF_6-derived model displays the latest arrival time around 7 years, intersects with the truth model around 19 years before it reaches a peak concentration at 31 years. SF_6-derived concentrations continue above the truth model until around the 57-year mark where the model intersects then declines below the truth model. We observe the

curves from the derived values for CFC11/SF_6 and CFC12/SF_6 overlap continuously throughout the plot. The concentrations for these models follow the truth model for the first 12 years before increasing above the truth model and display a peak contaminant concentration at approximately 27 years. Declining concentrations intersect with the truth model for a final time around 55 years. We observe the tritium-derived model above the CFC11/SF_6 and CFC12/SF_6 curves before reaching a peak concentration around 22 years. This model converged with the truth model around 37 years and intersects the truth model around 42 years.

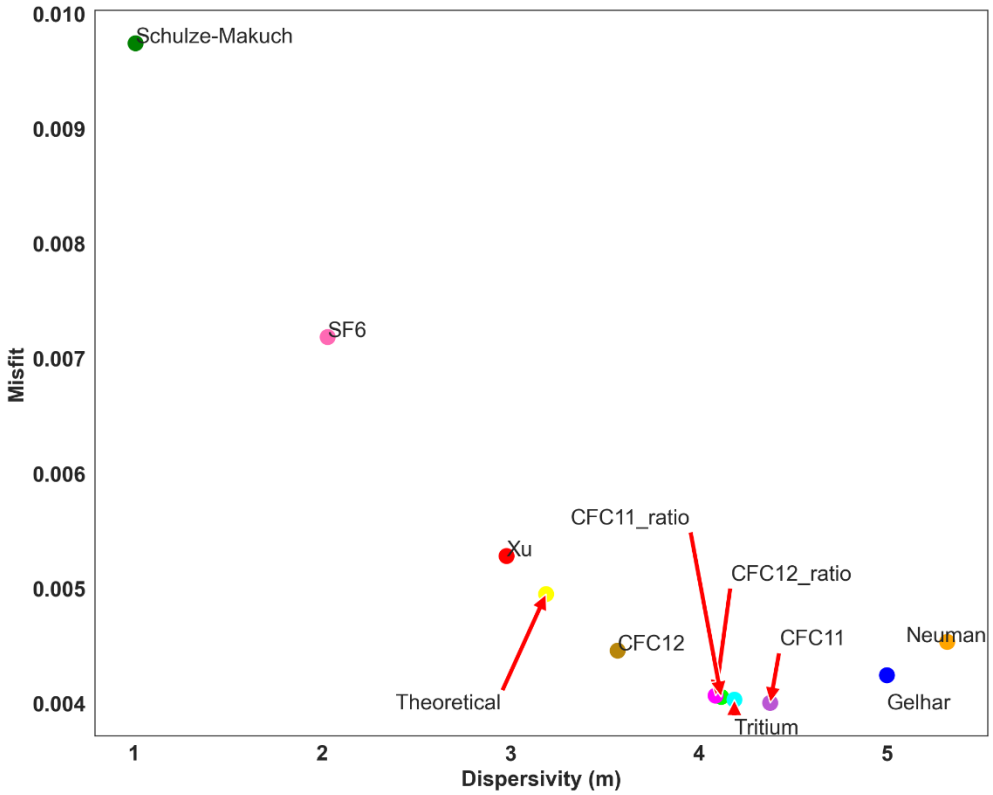

Figure 15 – Pulse inlet boundary condition, full-time series misfit plot displaying the misfit value on the y-axis and the tracer-derived, theoretical, and empirical values of longitudinal dispersivity (m) on the x-axis.

The misfit plot in figure 15 addresses the misfit quantification of the residuals for dispersivity values estimated using the full-time series. The largest misfit was for dispersivity from Schulze-Makuch with a misfit of 0.009. Tracer-derived values for the four cases: CFC11, tritium, CFC11 ratio, and CFC12 ratio display the best-fit with a misfit of 0.0040, 0.0041, and 0.0041, respectively.

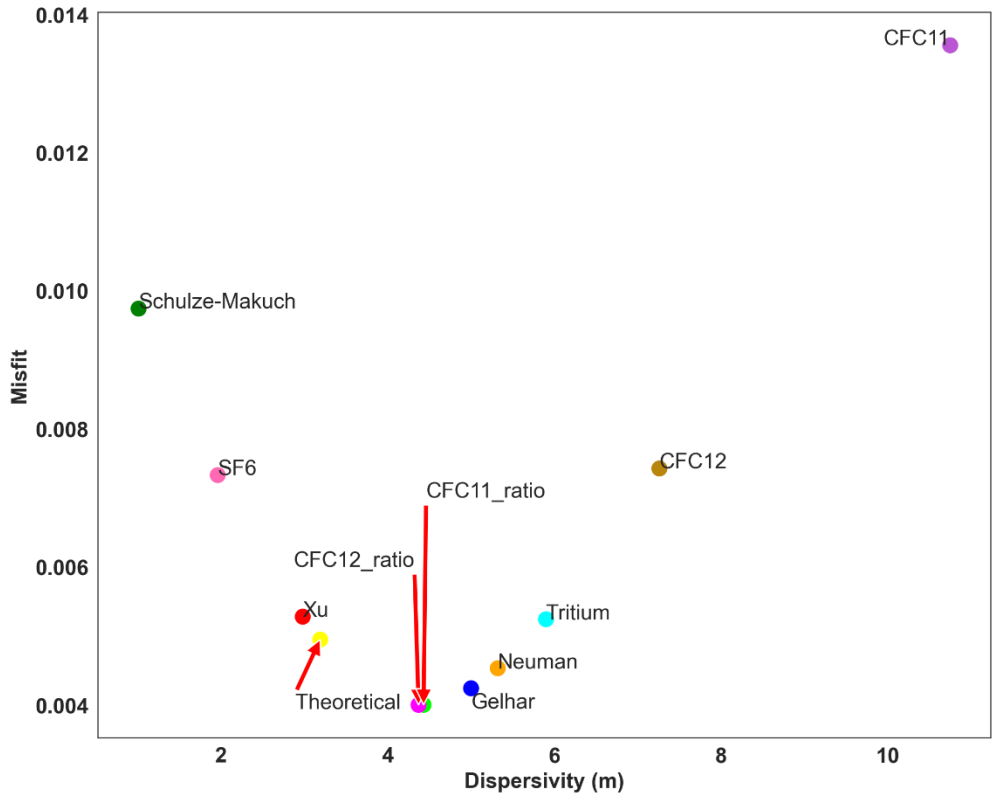

Figure 16 - Pulse inlet boundary condition, 2021 single-time series misfit plot displaying the misfit value on the y-axis and the tracer-derived, theoretical, and empirical values of longitudinal dispersivity (m) on the x-axis.

The misfit plot in figure 16 addresses the misfit quantification of the residuals for dispersivity values estimated from the 2021 single-time series. The CFC11-derived and the empirically calculated Schulze-Makuch values of dispersivity displays the largest misfit with a value of 0.0136 and 0.0901, respectively. CFC11 and CFC12 ratio-derived values display the best fit with a misfit of 0.0040.

Table 7 – Pulse inlet, full-time series chi-squared goodness of fit values.

Longitudinal Dispersivity Source	χ^2
Theoretical Calculation - 3.19 m	4.0×10^{-3}
Gelhar - 5.0 m	2.0×10^{-3}
Neuman & Zhang - 5.32 m	3.0×10^{-3}
Xu & Eckstein - 2.98 m	4.0×10^{-3}
Schulze-Makuch - 1.01m	1.1×10^{-2}
CFC11, Full Time Series - 4.38 m	2.0×10^{-3}
CFC12, Full Time Series - 3.57 m	3.0×10^{-3}
Tritium, Full Time Series - 4.19 m	2.0×10^{-3}
SF_6, Full Time Series - 2.03 m	7.0×10^{-3}
CFC11 ratio, Full Time Series - 4.12 m	2.0×10^{-3}
CFC12 ratio, Full Time Series - 4.09m	2.0×10^{-3}

Table 7 displays the values of the chi-squared goodness of fit test (equations 18 & 19) to determine how well the observed models for values dispersivity derived from the full-time series, and theoretical and empirically derived values, fit our observed truth model. The critical chi-squared value is 46.19 with 32 degrees of freedom. The chi-square test statistic for all observed models fails to reject the null hypothesis, and there is no significant difference between the individual observed models.

Table 8 – Pulse inlet, single-time series chi-squared goodness of fit values.

Longitudinal Dispersivity Source	χ^2
Theoretical Calculation - 3.19 m	4.0×10^{-3}
Gelhar - 5.0 m	2.0×10^{-3}
Neuman & Zhang - 5.32 m	3.0×10^{-3}
Xu & Eckstein - 2.98 m	4.0×10^{-3}
Schulze-Makuch - 1.01m	1.1×10^{-2}
CFC11, Single Time Series - 10.75 m	9.9×10^{-2}
CFC12, Single Time Series - 7.26 m	1.1×10^{-2}
Tritium, Single Time Series - 5.89 m	4.00×10^{-3}
SF_6, Single Time Series - 1.96 m	7.0×10^{-3}
CFC11 ratio, Single Time Series - 4.43 m	2.0×10^{-3}
CFC12 ratio, Single Time Series - 4.37 m	2.0×10^{-3}

Table 8 displays the values of the chi-squared goodness of fit test (equations 18 & 19) to determine how well the observed models for values dispersivity derived from the full-time series, and theoretical and empirically derived values, fit our observed truth model. The critical chi-squared value is 46.19 with 32 degrees of freedom. The chi-square test statistic for all observed models fails to reject the null hypothesis, and there is no significant difference between the individual observed models.

6. Discussions and Limitations

Discussion

A major purpose of this study was to evaluate if the value of an effective field-scale longitudinal dispersivity could be derived from anthropogenically applied environmental tracers sampled from groundwater systems over limited spatial and temporal scales. This study includes a new method of using the concentration ratios of CFC11 and CFC12 over SF_6 to mimic a distinct concentration peak analogous to tritium concentrations that are decaying out of our subsurface systems (Figure 1). We compared these tracer-derived values to theoretical and empirically derived values of dispersivity reasonable for our synthetic structure (Figure 6). We assessed the ability of these tracer-derived dispersivity coefficients to reproduce transport of a synthetic contaminant through a synthetic, heterogeneous, 3-dimensional flow field with two different boundary conditions and quantified the residuals to our truth model (Figures 10, 11, 15 & 16). We then calculated the chi-squared goodness of fit test statistics from these observed models to our expected truth model for our new boundary conditions (Tables 5, 6, 7, & 8) to determine if there was a method that performed the best.

We compare the tracer-derived values from the full time series to the single time series representative of 2021 (Tables 3 & 4, Figure 6). CFC11-derived dispersivity values show the largest percent difference of 146% with values of 4.38 m and 10.75 m from the full and single sample, respectively. CF12-derived values have a 103% difference between the full and single-time series with dispersivity values between 3.58 m and 7.26 m, respectively. Tritium-derived values display a 41% difference with values of 4.19 m and 5.89 m from the full and single-time series, respectively. SF_6-derived values display a -3% difference due to the values decreasing from 2.03 m to 1.96 m between the full and single-

time series. The ratios of CFC11/SF_6 and CFC12/SF_6 display less than a 10% difference between the full and single-time series. The CFC11/SF_6-derived value of dispersivity from the full-time series is 4.12 m, compared to the single-time series value of 4.43 (8% difference). CFC12/SF_6 -derived dispersivity value from the full-time series is 4.09 m, compared to the single-time series value of 4.43 with a 7% difference (Figure 6). All tracer-derived values were within the same order of magnitude compared to the theoretically and empirically derived values (Figure 6).

We assessed the ability of these optimized dispersivity values to reproduce transport of a contaminant in our synthetic aquifers with two different boundary conditions. Misfit plots and chi-squared test statistics were able to quantify which tracers, and the ratios therein, were able to best fit our truth model. From the breakthrough curves for the step function inlet boundary condition (Figures 7, 8, & 9) we observe that all models follow the truth model at early time steps, but at the 25-year mark our observed models begin to over-estimate the truth model signifying that there is significant bias in the observed models between 25 and 75 years. All observed models reach a peak maximum concentration earlier than our truth model. The full-time series tracer-derived values from CFC11, CFC11 ratio, CFC12 ratio, and tritium best fit our truth model with misfit values between 0.130 and 0.135. (Figure 10). The single-time CFC11-derived value of dispersivity for the same boundary condition showed the largest misfit from our truth model at 0.172 (Figure 11). The CFC12-tracer-derived values for the full-time series have a misfit of around 0.137 and 0.140 for the single-time series. SF_6-derived values from both the full and single-time series consistently had a misfit quantification of 0.150. Tritium-derived values from the same misfit plots remained below 0.135 for both time series, showing a good fit in both circumstances. The chi-squared goodness of fit tests from both the full and single-time series (Tables 5 & 6) concluded that there was no significant difference between all observed models and the truth model. This finding shows that all tracer-derived values of longitudinal dispersivity used to test the ability to reproduce transport in our system were able to fit our truth model, and there is no statistical evidence that one tracer-derived value, from both the full and single-time series, performed best.

The breakthrough curves for the pulse inlet boundary condition (Figures 12, 13, & 14) follow the truth model at early time steps, but we observe the same anomaly at the 25-

year mark where the observed models begin over-estimate the truth model. All observed models reach a peak concentration and flush out of our system earlier than truth model. We see the same conditional bias that was present in the step function boundary condition. This conditional bias could be due to our assumption of Fickian-flow within all systems. Misfit quantification from the pulse inlet boundary condition shows that the CFC11-derived value of dispersivity performed well for the full-time series (Figure 15) with a misfit of 0.004, and the worst for the single-time series (Figure 16) with a misfit value of 1.4×10^{-2}. The tritium-derived value is approximately equal to the CFC11-derived misfit value for the full-time series with a misfit value of 0.004 and increases to 0.005 for the single-time series (Figure 16). CFC12-derived values of dispersivity for the full-time series shows a low misfit value at 0.003 and then increases for the single-time series with a misfit value of 0.007. SF_6- derived dispersivity misfit values do not fit the truth model well for both the full and single time series with a consistent misfit value of 0.007 (Figure 15 & 16). The chi-squared goodness of fit tests from both the full and single-time series (Tables 7 & 8) shows that there was no significant difference between all observed models and the truth model. Due to this, we cannot definitively state that one tracer-derived value of dispersivity, from either the full or single-time series, statistically fit our truth model best.

Our results indicate that environmental tracers can be useful in estimating effective dispersion coefficients for reactive transport models over longer length and time scales than traditional applied tracer studies. All methods provided a result that was not significantly diverse. Dispersivity values derived from CFC11/SF_6 and CFC12/SF_6 displayed small residuals for both boundary conditions for the full and single-time series (Figures 10, 11, 15 & 16) and could be considered are more robust method. This is attributed to the small percent difference between the full and single-time series optimized dispersivity values (Figure 6). This could signify that a spatially limited, single-time sample of CFC11, CFC12, SF_6, and tritium can yield a reasonable field-scale value of longitudinal dispersivity.

Caveats and limitations

While all tracer-derived values of longitudinal dispersivity were able to predict an independent contaminant breakthrough in our synthetic aquifer, this study only looks at

one 3D configuration that is uniform. Different representative elementary volumes with different medium configurations could lead to contrasting outcomes. The total porosity of a medium represents the ratio of the volume of voids to the total volume of the rock or soil sample. The effective porosity refers to the amount of pore space available for fluid transmission through interconnected pore space relative to the total volume and can vary with the direction of flow within a given system. The impacts of effective porosity and hydraulic conductivity in different geologic mediums would influence the aquifers velocity, thereby influencing the dispersion parameter. Directionally dependent dispersivity is a common generalization where we expect the flow to be parallel to the medium in the x direction. Longitudinal dispersivity would not be prominent where there is flow that is perpendicular to the medium in the x direction and transverse dispersivity could be the dominant parameter. We only considered one well location for this theoretical study. Varying locations of the well would have different arrival times of the environmental tracers and could lead to different PEST optimized values of longitudinal dispersivity. This model is tuned so that the environmental tracers pass through our synthetic well within the specified period. In the field, aquifers with groundwater ages older than 60 years might not perform as well, and samples obtained from aquifers at larger distances may not provide the same information. This study only considered a fully confined aquifer and did not look at unconfined aquifers where above ground recharge could influence the total concentrations of all environmental tracers. These results would be valid for groundwater less than 60 years old with limited above ground recharge. This could lead to age, distance, and velocity ranges where this method of predicting field-scale values of longitudinal dispersivity with a single time series of environmental tracers are limited.

7. Conclusions

In this study, we incorporated a suite of environmental tracer concentrations directly into numerical reactive transport of a 3D heterogeneous synthetic model and sampled them over a limited spatial and temporal scale. Flux-averaged concentrations of these environmental tracers are used as observation datasets to calibrate simplified 3D homogeneous aquifer models with PEST to estimate a field-scale of longitudinal dispersivity. We calculated field-scale values of longitudinal dispersivity from theoretical

and empirical equations to ensure that the tracer-derived values obtained from PEST optimizations were reasonable in comparison. We then assessed the ability of full and single-time series tracer-derived values to predict contaminant transport of an independent contaminant through the 3D heterogeneous synthetic flow field with a set of two different inlet boundary conditions. The main conclusions from this study are:

- Tracer-derived values of longitudinal dispersivity from CFC11, CFC12, SF_6, and tritium between 1.96 m and 10.75 m are within the same order of magnitude compared to theoretical and empirically derived values of dispersivity calculated values between 1.01 m to 5.32 m.
- Tracer-derived values of longitudinal dispersivity from CFCs/SF_6 ratios from 4.09 m to 4.43 m are reasonable compared to theoretical and empirically calculated values between 1.01 m to 5.32 m.
- CFCs/SF_6 ratios can derive reasonable values of longitudinal dispersivity from a single time-series.
- All environmental tracers, including CFCs/SF_6 ratios, can derive reasonable values of longitudinal dispersivity from a limited time-series.

These results show the potential for a new technique of sampling environmental tracer concentrations over limited spatial and temporal scales, including the method of using the ratios of CFC11/SF_6 and CFC12/SF_6, to constrain a reasonable field-scale value of longitudinal dispersivity in certain aquifer systems. This new method of utilizing multiple environmental tracers over a limited time series could be an easy, inexpensive, and effective solution in quantifying field-scale longitudinal dispersivity and reduce parameter uncertainty in groundwater/contamination transport models.

References

Aeschbach-Hertig, W., Peeters, F., Beyerle, U., and Kipfer, R., 2000, Paleotemperature reconstruction from noble gases in groundwater accounting for equilibration with entrapped air: Nature, v. 405, p. 1040–1044.

Bear, J., and Bachmat, Y., 1967, A Generalized Theory On Hydrodynamic Dispersion In Porous Media: Int. Union Geod. Geophys. Publ., v. 72, p. 7–17.

Bredehoeft, J., 2005, The conceptualization model problem - Surprise: Hydrogeology Journal, v. 13, p. 37–46, doi:10.1007/s10040-004-0430-5.

Chambers, L.A., Gooddy, D.C., and Binley, A.M., 2018, Use and application of CFC-11, CFC-12, CFC-113 and SF6 as environmental tracers of groundwater residence time: A review: Geoscience Frontiers, v. 10, p. 1643–1652, doi:10.1016/j.gsf.2018.02.017.

Cook, P.G., 2000, Environmental Tracers in Subsurface Hydrology:, doi:10.1007/978-1-4615-4557-6.

Correa, A.C.D.F., 1988, Application of the Unit Step Function to Transient Flow Problems with Time-Dependent Boundary Conditions: Numerical Methods for Partial Differential Equations, v. 63, p. 363–791.

Doherty, J., 2007, Use of PEST and Some of its Utilities in Model Calibration and Predictive Error Variance Analysis : - A Roadmap prepared by:

Doherty, J., and Hunt, R., 2010, Approaches to highly parameterized inversion: a guide to using PEST for groundwater-model calibration: U. S. Geological Survey Scientific Investigations Report 2010-5169, p. 70, http://pubs.usgs.gov/sir/2010/5169/.

Egboka, B.C.E., Cherry, J.A., Farvolden, R.N., and Frind, E.O., 1983, Migration of contaminants in groundwater at a landfill: A case study. 3. Tritium as an indicator of dispersion and recharge: Journal of Hydrology, v. 63, p. 51–80, doi:10.1016/0022-1694(83)90223-8.

EPA 2013, 2011, EPA 2013: v. 2011, https://www3.epa.gov/ceampubl/learn2model/part-two/onsite/longdisp.html (accessed March 2022).

Gardner, W.P., Hammond, G., and Lichtner, P., 2015, High Performance Simulation of Environmental Tracers in Heterogeneous Domains: Groundwater, v. 53, p. 71–80, doi:10.1111/gwat.12148.

Gardner, W.P., Susong, D.D., Solomon, D.K., and Heasler, H.P., 2011, A multitracer approach for characterizing interactions between shallow groundwater and the hydrothermal system in the Norris Geyser Basin area, Yellowstone National Park: Geochemistry, Geophysics, Geosystems, v. 12, p. 1–17, doi:10.1029/2010GC003353.

Gelhar, L.W., 1993, Stoichastic Subsurface Hydrology: Prentice Hall, Upper Saddle River, NJ. 28.

Gelhar, L.W., and Axness, C.L., 1983, Three-dimensional stochastic analysis of macrodispersion in aquifers: Water Resources Research, v. 19, p. 161–180, doi:10.1029/WR019i001p00161.

Gelhar, L.W., Welty, C., and Rehfeldt, K.R., 1992, A critical review of data on field-scale dispersion in aquifers: Water Resources Research, v. 28, p. 1955–1974, doi:10.1029/92WR00607.

Gupta, H. V., Clark, M.P., Vrugt, J.A., Abramowitz, G., and Ye, M., 2012, Towards a comprehensive assessment of model structural adequacy: Water Resources Research, v. 48, p. 1–16, doi:10.1029/2011WR011044.

Hammond, G.E., Lichtner, P.C., Lu, C., and Mills, R.T., 2012, PFLOTRAN: Reactive flow & transport code for use on laptops to leadership-class supercomputers: Groundwater Reactive Transport Models, v. 5, p. 141–159, doi:10.2174/978160805306311201010141.

Ingebritsen, S.E., and Sanford, W.E., 1998, Groundwater in geologic processes:, doi:10.1111/j.1468-8123.2009.00253.x.

Jensen, K.H., Bitsch, K., and Bjerg, P.L., 1993, Large-scale dispersion experiments in a sandy aquifer in Denmark: Observed tracer movements and numerical analyses: Water Resources Research, v. 29, p. 673–696, doi:10.1029/92WR02468.

Kagabu, M., Matsunaga, M., Ide, K., Momoshima, N., and Shimada, J., 2017, Groundwater age determination using85Kr and multiple age tracers (SF6, CFCs, and3H) to elucidate regional groundwater flow systems: Journal of Hydrology: Regional Studies, v. 12, p. 165–180, doi:10.1016/j.ejrh.2017.05.003.

Khan, A.U.H., and Jury, W.A., 1990, A laboratory study of the dispersion scale effect in column outflow experiments: Journal of Contaminant Hydrology, v. 5, p. 119–131,

doi:10.1016/0169-7722(90)90001-W.

Konikow, L.F., and Grove, D.B., 1977, Derivation of equations describing solute transport in ground water.:

Leray, S., de Dreuzy, J.R., Bour, O., Labasque, T., and Aquilina, L., 2012, Contribution of age data to the characterization of complex aquifers: Journal of Hydrology, v. 464–465, p. 54–68, doi:10.1016/j.jhydrol.2012.06.052.

Li, G., 2011, Spatially varying dispersion to model breakthrough curves: Ground Water, v. 49, p. 584–592, doi:10.1111/j.1745-6584.2010.00777.x.

Lovanh, N., Zhang, Y.-K., Heathcote, R.C., and Alvarez, P.J.J., 2000, Guidelines to Determine Site-Specific Parameters for Modeling the Fate and Transport of Monoaromatic Hydrocarbons in Groundwater: University of Iowa,.

Neuman, S.P., and Zhang, Y. -K, 1990, A quasi-linear theory of non-Fickian and Fickian subsurface dispersion: 1. Theoretical analysis with application to isotropic media: Water Resources Research, v. 26, p. 887–902, doi:10.1029/WR026i005p00887.

NOAA Global Monitoring Laboratory - Halocarbons and other Atmospheric Trace Species, https://gml.noaa.gov/hats/combined/CFC11.html (accessed May 2022).

Novakowski, K.S., Evans, G. V., Lever, D.A., and Raven, K.G., 1985, A Field Example of Measuring Hydrodynamic Dispersion in a Single Fracture: Water Resources Research, v. 21, p. 1165–1174, doi:10.1029/WR021i008p01165.

Nussbaumer, R., Grégoire Mariethoz, ·, Gloaguen, · Erwan, and Holliger, K., 2018, Which Path to Choose in Sequential Gaussian Simulation: Math Geosci, v. 50, p. 97–120, doi:10.1007/s11004-017-9699-5.

Pang, L., and Hunt, B., 2001, Solutions and verification of a scale-dependent dispersion model: Journal of Contaminant Hydrology, v. 53, p. 21–39, doi:10.1016/S0169-7722(01)00134-6.

Robertson, W.D., and Cherry, J.A., 1989, Tritium as an indicator of recharge and dispersion in a groundwater system in central Ontario: Water Resources Research, v. 25, p. 1097–1109, doi:10.1029/WR025i006p01097.

Safikhani, M., Asghari, O., and Emery, X., 2017, Assessing the accuracy of sequential gaussian simulation through statistical testing: Stochastic Environmental Research and Risk Assessment, v. 31, p. 523–533, doi:10.1007/S00477-016-1255-1.

Scheidegger, A.E., 1961, General theory of dispersion in porous media: Journal of Geophysical Research, v. 66, p. 3273–3278, doi:10.1029/jz066i010p03273.

Schulze-Makuch, 2005, Longitudinal Dispersivity Data and Implications for Scaling Behavior: v. 43, p. 443–456.

Shapiro, A.M., and Cvetkovic, V.D., 1988, Stochastic analysis of solute arrival time in heterogeneous porous media: Water Resources Research, v. 24, p. 1711–1718, doi:10.1029/WR024i010p01711.

Singh, M.K., Mahato, N.K., and Singh, P., 2011, Longitudinal dispersion with constant source concentration along unsteady groundwater flow in finite aquifer: analytical solution with pulse type boundary condition: Natural Science, v. 03, p. 186–192, doi:10.4236/ns.2011.33024.

Suckow, A., 2014, The age of groundwater - Definitions, models and why we do not need this term: Applied Geochemistry, v. 50, p. 222–230, doi:10.1016/j.apgeochem.2014.04.016.

Sudicky, E.A., 1988, A natural gradient experiment on solute transport in a sand aquifer: Spatial variability of hydraulic conductivity and its role in the dispersion process: Water Resources Research, v. 24, p. 1209–1210, doi:10.1029/WR024i007p01209.

Sudicky, E.A., and Illman, W.A., 2011, Lessons learned from a suite of CFB Borden experiments: Ground Water, v. 49, p. 630–648, doi:10.1111/j.1745-6584.2011.00843.x.

Xu, M., and Eckstein, Y., 1995, Use of Weighted Least-Squares Method in Evaluation of the Relationship Between Dispersivity and Field Scale: Groundwater, v. 33, p. 905–908, doi:10.1111/j.1745-6584.1995.tb00035.x.

Zhang, R., 1996, Applied Contaminant Transport Modeling: Theory and Practice: Journal of Environment Quality, v. 25, p. 927, doi:10.2134/jeq1996.00472425002500040045x.

Zuber, A. et al., 2005, Groundwater dating with 3H and SF6 in relation to mixing patterns, transport modelling and hydrochemistry: Hydrological Processes, v. 19, p. 2247–2275, doi:10.1002/hyp.5669.

Appendix

1940 – 2021 Environmental Tracer Aqueous Concentrations

Year	CFC11	CFC12	CFC113	SF6	H3
1940	0	2.17E-15	0	0	3.04E-15
1941	0	2.71E-15	0	0	3.04E-15
1942	0	3.79E-15	0	0	3.04E-15
1943	0	4.88E-15	0	0	3.04E-15
1944	0	6.50E-15	0	0	3.04E-15
1945	2.09E-15	9.21E-15	0	0	3.04E-15
1946	2.09E-15	1.25E-14	0	0	3.04E-15
1947	2.09E-15	1.84E-14	0	0	3.04E-15
1948	4.18E-15	2.60E-14	0	0	3.04E-15
1949	8.35E-15	3.31E-14	0	0	3.04E-15
1950	1.46E-14	4.12E-14	0	0	3.35E-14
1951	2.11E-14	4.99E-14	0	0	4.97E-15
1952	3.15E-14	5.96E-14	0	0	1.62E-14
1953	4.61E-14	6.94E-14	0	1.57E-17	1.34E-14
1954	6.30E-14	8.13E-14	0	1.57E-17	5.73E-14
1955	8.60E-14	9.43E-14	0	1.57E-17	6.00E-14
1956	1.11E-13	1.09E-13	0	1.57E-17	1.63E-14
1957	1.43E-13	1.27E-13	0	1.96E-17	2.36E-14
1958	1.70E-13	1.45E-13	0	1.96E-17	1.09E-13
1959	1.97E-13	1.65E-13	0	1.96E-17	3.27E-13
1960	2.31E-13	1.90E-13	0	1.96E-17	1.73E-13
1961	2.77E-13	2.17E-13	6.45E-16	2.35E-17	9.61E-14
1962	3.38E-13	2.48E-13	1.93E-15	2.74E-17	6.48E-14
1963	4.09E-13	2.84E-13	3.22E-15	3.14E-17	3.46E-14
1964	4.95E-13	3.27E-13	5.16E-15	3.53E-17	2.35E-14
1965	5.94E-13	3.76E-13	7.09E-15	4.31E-17	2.41E-14
1966	7.03E-13	4.29E-13	9.61E-15	5.10E-17	2.27E-14
1967	8.23E-13	4.89E-13	1.28E-14	5.88E-17	2.16E-14
1968	9.61E-13	5.57E-13	1.73E-14	7.06E-17	9.80E-15
1969	1.12E-12	6.33E-13	2.19E-14	8.23E-17	1.03E-14
1970	1.30E-12	7.15E-13	2.70E-14	9.02E-17	1.13E-14
1971	1.50E-12	8.04E-13	3.34E-14	1.02E-16	8.64E-15
1972	1.73E-12	9.00E-13	4.04E-14	1.18E-16	6.52E-15
1973	1.98E-12	1.01E-12	4.82E-14	1.33E-16	8.34E-15
1974	2.26E-12	1.12E-12	5.78E-14	1.49E-16	8.55E-15
1975	2.53E-12	1.24E-12	6.87E-14	1.73E-16	5.38E-15
1976	2.80E-12	1.34E-12	8.03E-14	1.96E-16	6.27E-15
1977	3.10E-12	1.44E-12	9.44E-14	2.27E-16	6.26E-15
1978	3.27E-12	1.53E-12	1.09E-13	2.59E-16	5.18E-15
1979	3.43E-12	1.61E-12	1.27E-13	2.98E-16	5.40E-15
1980	3.63E-12	1.70E-12	1.46E-13	3.45E-16	4.43E-15

1981	3.78E-12	1.78E-12	1.67E-13	3.92E-16	3.52E-15
1982	3.94E-12	1.86E-12	1.88E-13	4.43E-16	4.49E-15
1983	4.15E-12	1.96E-12	2.13E-13	4.98E-16	4.33E-15
1984	4.31E-12	2.03E-12	2.44E-13	5.49E-16	4.24E-15
1985	4.55E-12	2.12E-12	2.83E-13	6.08E-16	4.90E-15
1986	4.76E-12	2.22E-12	3.12E-13	6.71E-16	4.26E-15
1987	5.02E-12	2.33E-12	3.59E-13	7.37E-16	4.15E-15
1988	5.28E-12	2.49E-12	4.10E-13	8.04E-16	2.37E-15
1989	5.45E-12	2.59E-12	4.50E-13	8.71E-16	2.14E-15
1990	5.53E-12	2.67E-12	4.88E-13	9.45E-16	2.20E-15
1991	5.59E-12	2.72E-12	5.22E-13	1.03E-15	2.04E-15
1992	5.64E-12	2.78E-12	5.41E-13	1.12E-15	1.85E-15
1993	5.66E-12	2.81E-12	5.44E-13	1.21E-15	2.45E-15
1994	5.64E-12	2.83E-12	5.50E-13	1.39E-15	2.43E-15
1995	5.60E-12	2.87E-12	5.46E-13	1.43E-15	2.08E-15
1996	5.57E-12	2.89E-12	5.45E-13	1.51E-15	2.52E-15
1997	5.54E-12	2.91E-12	5.42E-13	1.61E-15	2.28E-15
1998	5.51E-12	2.93E-12	5.37E-13	1.68E-15	1.76E-15
1999	5.47E-12	2.94E-12	5.33E-13	1.76E-15	1.76E-15
2000	5.44E-12	2.95E-12	5.30E-13	1.84E-15	1.76E-15
2001	5.41E-12	2.95E-12	5.27E-13	1.92E-15	1.76E-15
2002	5.36E-12	2.96E-12	5.23E-13	2.01E-15	1.76E-15
2003	5.31E-12	2.95E-12	5.18E-13	2.10E-15	1.76E-15
2004	5.27E-12	2.95E-12	5.13E-13	2.19E-15	1.76E-15
2005	5.23E-12	2.94E-12	5.09E-13	2.28E-15	1.76E-15
2006	5.18E-12	2.93E-12	5.04E-13	2.37E-15	1.76E-15
2007	5.13E-12	2.92E-12	4.99E-13	2.48E-15	1.76E-15
2008	5.09E-12	2.91E-12	4.94E-13	2.60E-15	1.76E-15
2009	5.05E-12	2.89E-12	4.90E-13	2.71E-15	1.76E-15
2010	5.01E-12	2.87E-12	4.86E-13	2.83E-15	1.76E-15
2011	4.97E-12	2.86E-12	4.82E-13	2.93E-15	1.76E-15
2012	4.93E-12	2.84E-12	4.77E-13	3.05E-15	1.76E-15
2013	4.90E-12	2.82E-12	4.72E-13	3.18E-15	1.76E-15
2014	4.88E-12	2.81E-12	4.68E-13	3.31E-15	1.76E-15
2015	4.85E-12	2.79E-12	4.65E-13	3.44E-15	1.76E-15
2016	4.83E-12	2.78E-12	4.61E-13	3.57E-15	1.76E-15
2017	4.81E-12	2.76E-12	4.58E-13	3.71E-15	1.76E-15
2018	4.79E-12	2.74E-12	4.54E-13	3.83E-15	1.76E-15
2019	4.75E-12	2.72E-12	4.49E-13	3.98E-15	1.76E-15
2020	4.69E-12	2.70E-12	4.45E-13	4.09E-15	1.76E-15
2021	4.69E-12	2.68E-12	4.45E-13	4.15E-15	1.76E-15